Wake encounters between two full-configuration UAM aircraft in forward flight: Aerodynamic response and implications for operational spacing

Da-bin Jung[a], Sang Min Son[a], Chan-Ho Song[a], Rho Shin Myong[a,b], Hakjin Lee[a,b,*]

[a]*School of Aerospace Engineering, Gyeongsang National University, Jinju, Gyeongnam 52828, South Korea*

[b]*Global Research Center for Aircraft Core Technology, Jinju, Gyeongnam 52528, South Korea*

[*]Author to whom correspondence should be addressed: hlee@gnu.ac.kr

Abstract

Wake encounters between urban air mobility (UAM) aircraft can alter the aerodynamic response of following aircraft because multirotor wakes are highly unsteady and may interact with both rotors and fuselage. However, the effects of downstream wake evolution on the aerodynamic response during wake encounters between two full-configuration UAM aircraft remain poorly understood. Thus, this study examines wake encounter effects between two full-configuration UAM aircraft in forward flight using the in-house vortex-based aerodynamic solver VALOR, which couples the nonlinear vortex lattice method for rotor aerodynamics, the source–doublet panel method for airframe aerodynamics, and the vortex particle method for wake convection. The wake generated by the leading aircraft convects downstream and impinges on the following aircraft, producing position-dependent variations in aerodynamic performance. Six cases are considered at a fixed streamwise separation of $x/R = 6$ by combining advance ratios of $\mu = 0.15$ and 0.23 with vertical separations of $z/R = 0$, -1, and -2. Results show that the advance ratio influences the wake convection path and thereby the relative encounter location between the wake and following aircraft. At $\mu = 0.15$, the mean thrust reductions are 29.12%, 25.17%, and 11.10%, whereas the corresponding reductions at $\mu = 0.23$ are 25.63%, 14.17%, and 7.70%. The maximum mean torque reduction is 8.02%. Additionally, the fuselage pressure distribution and pitching moment vary with the position of the wake relative to the following aircraft, suggesting that wake effects extend beyond the rotor disks. These findings demonstrate that the aerodynamic response of following UAM aircraft during wake encounters must be assessed by considering both the wake convection path and wake position relative to the following aircraft.

Keywords: Urban air mobility; wake encounter; wake interaction; aerodynamic response; vortex particle method

1. Introduction

Tip vortices shed from aircraft wings and rotor blades represent a primary source of wake disturbance in forward flight. These coherent vortical structures are convected downstream and generate a velocity field that may persist over considerable distances depending on vortex strength, wake transport, and decay characteristics [1]. When a following aircraft enters this disturbed wake region, the induced velocity field modifies the local inflow over lifting surfaces, rotor blades, and airframe components, resulting in unsteady aerodynamic loads and changes in attitude response or control demand. Such events are referred to as wake encounters, where the wake generated by a leading aircraft induces aerodynamic disturbances on a following aircraft. Wake encounters have been associated with hazardous flight conditions and wake-turbulence-related incidents, particularly during takeoff, landing, and closely spaced operations. Wake encounters thus represent not only a wake dynamics problem but also an aerodynamic disturbance that may have implications for operational safety and aircraft separation. Given these potential safety implications, wake encounter and vortex behaviors have been extensively investigated for fixed-wing aircraft and rotorcraft [2,3].

In conventional air traffic operations, wake turbulence separation is defined through prescriptive distance- and time-based minima. At the international level, ICAO Doc 4444 (PANS-ATM) provides the relevant procedures and minima for wake turbulence separation [4]. In the United States, FAA Order JO 7110.65 specifies air traffic control procedures, including wake turbulence separation minima for radar, approach, and departure operations [5]. In Europe, wake turbulence separation is addressed within the EASA ATM/ANS regulatory framework under Regulation (EU) 2017/373, as amended, and is further refined through the EUROCONTROL RECAT-EU and RECAT-EU-PWS schemes [6–8]. Notably, these separation criteria are primarily based on wake turbulence categories and aircraft-pair characteristics, including maximum take-off mass, wingspan, and wake resistance of the following aircraft. They have provided an operational basis for reducing wake encounter risk in conventional airport environments. However, these criteria were developed mainly for fixed-wing aircraft and conventional rotorcraft and do not account for the wake characteristics of emerging urban air mobility (UAM) aircraft characterized by multiple propellers, compact rotor arrangements, and vertical takeoff and landing (VTOL) capability. Although regulatory frameworks for UAM aircraft are being developed, vehicle-specific wake encounter criteria and separation minima for dense UAM operations remain to be established [9]. Therefore, before extending conventional wake separation concepts to UAM operations, UAM wake characteristics and the aerodynamic response of following UAM aircraft during wake encounters must be clarified.

UAM aircraft differ from conventional helicopters not only in configuration but also in their intended operating environment. A conventional helicopter is typically dominated by a large main-rotor wake, whereas many UAM configurations employ multiple smaller propellers distributed across a compact airframe to generate the required lift while satisfying size constraints [10]. This arrangement generally results in high disk loading and strong interactions among propeller wakes. Notably, the vortical structures shed from individual propellers may interact, merge, and distort as they are convected downstream [11–13]. Consequently, UAM wake dynamics are highly complex, with multiple interacting propeller wakes producing a nonuniform wake field that varies with vehicle configuration and flight condition. When a following UAM aircraft encounters such a wake, the incoming disturbance may simultaneously affect multiple propeller disks and airframe surfaces, producing unsteady changes in propeller loading, fuselage pressure distribution, and aerodynamic moment response. This issue becomes particularly important for UAM operations because these aircraft are expected to perform frequent takeoff, landing, approach, and departure operations at low altitude near vertiports and within densely populated urban areas. In these phases, under limited altitude and control margins, wake-induced load fluctuations may represent important aerodynamic disturbances for subsequent assessments of flight-dynamic response and operational safety. Therefore, wake encounters for UAM aircraft should be treated as a coupled problem involving multipropeller wake dynamics and full-aircraft aerodynamic response.

Previous studies relevant to the wake encounter problem in UAM aircraft can be divided into two groups. The first group focuses on wake generation and interactional aerodynamics of UAM or multirotor configurations. Because multiple rotors are closely arranged in such aircraft, the wakes generated by individual rotors interact, producing nonuniform inflow, wake distortion, load variations, and changes in pitching and rolling moments. Yoon et al. [14] performed high-fidelity detached eddy simulation (DES) with Spalart-Allmaras turbulence model to investigate the effects of rotor spacing and wing and fuselage components on the vertical force and aerodynamic efficiency of a generic quad tilt-rotor configuration in hover. Hwang et al. [15] performed unsteady Reynolds-averaged Navier–Stokes (RANS) simulations with an unstructured overset-mesh technique for a quadrotor unmanned aerial vehicle (UAV) with a fuselage in hover and forward flight, showing that the wake from the upstream rotor may affect the loading of the downstream rotor, as well as the pitch and rolling moments, depending on rotor arrangement (e.g., square or diamond). With the development of UAM and electric VTOL aircraft, wake dynamics and aerodynamic interference have been explored for more complex configurations. Ventura Diaz et al. [16] conducted a loose coupling of CAMRAD II and RANS solver to examine the effects of rotor overlap distance and airframe on the aerodynamic loads, aerodynamic efficiency, and rotor wake geometry

of a National Aeronautics and Space Administration (NASA) side-by-side UAM aircraft. Alvarez and Ning [17] used a vortex method to predict multirotor aerodynamic interactions and highlighted its ability to effectively capture the thrust drop and unsteady loading caused by rotor–rotor wake interactions. Caprace et al. [18] investigated rotor–airframe interaction for a generic quadcopter in forward flight and showed that the airframe exerts a notable influence on both the aerodynamic loads and near-wake structure. Caprace and Ning [19] performed large eddy simulations (LESs) to study the wake structures of a quadcopter, side-by-side helicopter, and tilt-wing configuration in cruise. Araghizadeh et al. [20] analyzed a side-by-side UAM configuration in ground effect using a coupled vortex method and acoustic analogy, showing that rotor–wake and rotor–ground interactions influence the rotor blade loads, wake structure, and aeroacoustic response. Overall, these studies established that UAM wake dynamics are highly complex because multiple propeller wakes interact with one another and with the airframe. However, they primarily focused on wake formation and interaction within a single vehicle, rather than wake encounters between two full-aircraft configurations.

The second group addresses wake encounters and aircraft response for fixed-wing aircraft, rotorcraft, and simplified multirotor pairs. Representative studies are summarized in Table 1. For fixed-wing configurations, wake encounters have been examined using simplified wing models and approach scenarios. For example, Stephan et al. [21] performed fully coupled hybrid RANS/LES simulations of a NACA 0012 rectangular wing model and analyzed the aerodynamic loads and moments on the trailing wing under wake encounter and formation-flight conditions. Höhne et al. [22] formulated a worst-case search approach for a following aircraft encountering wake vortices generated by heavy transport aircraft and identified critical encounter geometries during approach. Researchers have also explored wake encounter problems involving rotorcraft and single-rotor wakes. Querinjean et al. [23] investigated the wake characteristics and encounter severity of an isolated rotor in forward flight. Lawrence and Padfield [24] performed flight-mechanics-based simulations to evaluate the wake encounter severity of a helicopter during final approach. For multirotor configurations, Wang and Low [25] investigated a simplified leader–follower multirotor pair by coupling computational fluid dynamics (CFD) with software-in-the-loop simulations using a PX4 attitude controller, focusing on the wake response and attitude-control behavior of the following multirotor. Although these studies provide valuable insights into the effects of wake encounters on aerodynamic loads, moments, and control response, as well as guidelines on encounter severity and critical encounters, their scope is limited to simplified wing models, fixed-wing approach scenarios, isolated rotor wakes, helicopter approach scenarios, or simplified multirotor pairs. In other words, a systematic aerodynamic analysis of wake encounters between two full-configuration UAM aircraft remains limited.

Table 1. Representative studies on wake encounter and aircraft response.

Paper Details	Model	Research focus
Stephan et al. [21] (2021)	Rectangular wing	Aerodynamic loads during wake encounters
Höhne et al. [22] (2004)	Fixed-wing aircraft	Critical encounter scenarios
Querinjean et al. [23] (2024)	Isolated rotor blade	Rotorcraft wake structure and encounter severity
Lawrence and Padfield [24] (2008)	Helicopter	Rotorcraft wake encounter severity
Wang and Low [25] (2021)	Multirotor without fuselage	Wake response and controller stability
Present study	Full-configuration side-by-side UAM aircraft	Aerodynamic response, fuselage loading, and wake dynamics

Overall, previous UAM wake studies have mainly focused on wake interactions within a single aircraft, whereas wake encounter studies have primarily considered conventional aircraft or simplified configurations. In contrast, wake encounters between full-configuration UAM aircraft require the simultaneous consideration of multiple interacting rotor wakes, airframe interference, long-distance wake propagation, and the resulting aerodynamic response of the following aircraft. Despite this complexity, systematic investigations of the aerodynamic influence of the wake from a leading UAM aircraft on both the rotors and airframe of a following aircraft remain limited.

To address these knowledge gaps, this study investigates wake encounters between two full-configuration side-by-side UAM aircraft in forward flight, focusing on wake evolution, rotor thrust and torque variation, fuselage pressure loading, and longitudinal moment response of the following aircraft. Both leading and following NASA side-by-side UAM aircraft are considered, characterized by multiple rotors, airframe surfaces, and fuselage geometry. Six wake encounter simulation cases with a fixed streamwise separation are constructed by combining two advance ratios and three vertical separation distances. The advance ratio influences the wake convection path and skew angle, whereas the vertical separation distance controls the position of the convected wake relative to the rotor disks and fuselage of the following aircraft. Simulations are performed using a vortex-based numerical framework coupling a nonlinear vortex lattice method (NVLM) for rotor blades, source–doublet panel method for airframe surfaces, and vortex particle method (VPM) for wake convection. The proposed approach is suitable for the wake encounter problem because it preserves coherent vortical wake structures over long downstream distances while evaluating their aerodynamic influence on the rotors and airframe surfaces of the following aircraft.

Before applying the method to the UAM wake encounter problem, two validation studies are performed: the first validation compares the velocity field induced by a single rotor wake with the experimental measurements of Heyson and Katzoff [26], and the second validation compares the tip vortex trajectories of the ROBIN helicopter model at different advance ratios [27]. The validated method is then applied to two UAM aircraft to simulate the wake generated by the leading aircraft, its downstream convection, and its aerodynamic influence on the following aircraft. The present analysis is limited to wake-induced aerodynamic loads and moments and does not include six-degree-of-freedom flight-dynamics simulation. Therefore, the present results are interpreted as wake-induced aerodynamic disturbances acting on the following aircraft rather than as predictions of its flight-dynamic response or stability. Overall, this study provides a detailed aerodynamic assessment of the performance changes experienced by a following UAM aircraft during wake encounter, including wake ingestion, rotor-load variation, airframe pressure fluctuation, and longitudinal moment response. Furthermore, by evaluating the dependence of these responses on the position of the following aircraft relative to the wake, this study provides an aerodynamic basis for future assessments of UAM separation distance.

2. Numerical methods

In the wake encounter problem, the rotor wake generated by the leading UAM aircraft is convected downstream and interacts with the rotor disks and airframe surfaces of the following aircraft. Therefore, a numerical method must be able to model the wake of the leading aircraft over long downstream distances and evaluate the resulting rotor blade loads and fuselage pressure response of the following aircraft. Computational efficiency is also crucial, as several cases with different advance ratios and vertical separation distances are considered. To satisfy these requirements, the in-house vortex-based aerodynamic solver VALOR (Vortex-based Aerodynamic simuLation cOde for Rotorcraft) is employed. The VALOR framework couples the NVLM for azimuthally nonuniform blade loading, a source–doublet panel method for pressure loading and aerodynamic moments on airframe components, and the VPM for downstream wake convection. The overall computational procedure and information exchange among the coupled aerodynamic models are summarized in Fig. 1.

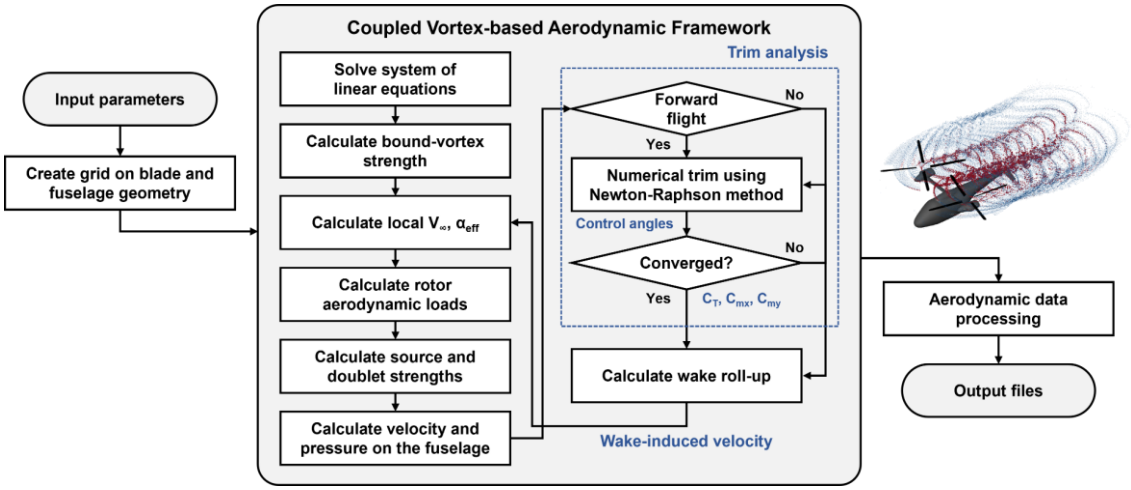

Fig. 1. Overall computational flowchart of the coupled vortex-based aerodynamic framework.

2.1 Coupled aerodynamic model

The aerodynamic loads acting on the rotor blades are calculated using the NVLM. The rotor blades are assumed to be thin lifting surfaces, and the mean camber surface of each blade is discretized in the chordwise and spanwise directions. A vortex ring element with constant circulation strength is placed on each blade panel, with the circulation strength determined by satisfying the no-penetration boundary condition at the collocation points on the blade surface. This condition is expressed as

$$\left(\mathbf{V}_{\infty}-\boldsymbol{\Omega}\times\mathbf{r}+\mathbf{V}_{ind,bound}+\mathbf{V}_{ind,wake}\right)\cdot\mathbf{n}=0 \tag{1}$$

where $\mathbf{V}_{\infty}$ is the freestream velocity, $\boldsymbol{\Omega}$ is the rotor angular velocity, $\mathbf{r}$ is the position vector from the rotor center to the collocation point, $\mathbf{V}_{ind,bound}$ is the velocity induced by bound vortices on the blade, $\mathbf{V}_{ind,wake}$ is the velocity induced by wake vortices, and $\mathbf{n}$ is the blade-surface normal vector.

Although the conventional vortex lattice method can efficiently determine the circulation distribution around thin lifting surfaces [28], it cannot account for the nonlinear aerodynamic characteristics of rotor blade sections. Therefore, in this study, the NVLM was coupled with airfoil lookup tables and a circulation-strength correction procedure. The local inflow velocity at each blade section is calculated as

$$\mathbf{V}_{inflow}=\mathbf{V}_{\infty}-\boldsymbol{\Omega}\times\mathbf{r}+\mathbf{V}_{ind,bound}+\mathbf{V}_{ind,wake} \tag{2}$$

In Eq. (2), the freestream velocity is prescribed according to the flight condition, while the rotational velocity is determined from the rotor angular velocity and the instantaneous position of each blade section. The velocity induced by bound vortices on the blade is evaluated from the circulation distribution determined by satisfying the no-penetration boundary condition in Eq. (1), whereas the velocity induced by wake vortices is calculated from

the shed wake represented by the VPM using the regularized Biot–Savart law described in Section 2.2. These velocity components are combined to obtain the local inflow velocity used to determine the effective angle of attack.

The effective angle of attack is then defined using the unit vectors $\mathbf{a}_1$ (tangential to the rotor plane) and $\mathbf{a}_3$ (normal to the rotor plane) as

$$\alpha_{eff} = \theta_{twist} + \theta_{pitch} - \tan^{-1}\left(\frac{\mathbf{V}_{inflow}\cdot\mathbf{a}_3}{\mathbf{V}_{inflow}\cdot\mathbf{a}_1}\right) \tag{3}$$

where θ_{twist} is the local blade twist angle, and θ_{pitch} is the local pitch angle, including collective and cyclic pitch inputs. The local inflow velocity and effective angle-of-attack are used as inputs to the airfoil lookup tables to obtain the lift and drag coefficients of each blade section. Subsequently, these sectional blade loads are integrated along the span to obtain the rotor thrust and torque. Unlike simplified rotor wake models that retain only tip vortices, the proposed framework uses vortex particles to represent the wake shed from the full-span blade trailing edge at every timestep, thereby capturing the wake dynamics and interactional phenomena in multirotor UAM configurations. The strength of the released vortex particles is determined from the bound circulation at the corresponding trailing-edge location through the Kutta condition and then convected downstream using VPM. The NVLM used in the present solver has been applied to various rotor aerodynamic problems, including wind turbines, helicopters, UAVs, and UAM aircraft. In these studies, the calculated rotor performance, blade loads, wake structures, and fuselage surface pressure distributions were compared with experimental data, high-fidelity CFD results, or published numerical results [20, 29–33]. Based on these validation results, the present solver is applied to the wake encounter analysis between two full-configuration UAM aircraft.

Unlike rotor blades, which can be treated as a thin lifting surface, the airframe, including the fuselage, cowlings, and tail surfaces, is modeled using the source–doublet panel method because these components have finite thickness and complex three-dimensional geometries [28]. The airframe surfaces are discretized into triangular panels, and constant source and doublet strengths are assigned to each panel to compute the local pressure distribution and aerodynamic loads. The doublet strengths are determined by satisfying the boundary condition on the body surface for each of the discretized triangular panels. After discretizing the fuselage surface into constant-strength triangular panels, the source–doublet boundary equation can be written as

$$\sum_{k=1}^{N} C_k \mu_k + \sum_{j=1}^{N_W} C_j \mu_{W,j} - \sum_{k=1}^{N} B_k \sigma_k = 0 \tag{4}$$

where N and N_W denote the numbers of body and wake panels, respectively; μ_k is the doublet strength on the k-

th body panel; $\mu_{W,j}$ is the doublet strength on the j-th wake panel; σ_k is the source strength on the k-th body panel; and C_k, C_j, and B_k are the corresponding influence coefficients.

The source strength is determined from the no-penetration boundary condition on the body surface. Considering the local kinematic velocity of the body surface, the source strength is defined as

$$\sigma = -\left(\mathbf{V}_{\infty} + \mathbf{V}_{rel} + \boldsymbol{\Omega} \times \mathbf{r}\right) \cdot \mathbf{n} \tag{5}$$

where σ is the source strength, and $\mathbf{V}_{rel}$ is the relative velocity of the surface. Because the airframe surfaces considered in this study do not exhibit rotational motion, the rotational velocity term is set to zero. However, the wake generated by the leading aircraft and the rotor wake of the following aircraft modify the local inflow around the fuselage, which, in turn, affects the fuselage surface pressure distribution and aerodynamic moments.

After determining the source and doublet strengths, the local velocity on the fuselage surface is calculated from the gradient of the velocity potential. Using the local velocity calculated on the panel surface, the pressure coefficient on the fuselage surface is derived from the unsteady Bernoulli equation as

$$C_p = 1 - \frac{\left|\mathbf{V}_{total}\right|^2}{\left|\mathbf{V}_{ref}\right|^2} - \frac{2}{\left|\mathbf{V}_{ref}\right|^2} \frac{\partial \phi}{\partial t} \tag{6}$$

where $\mathbf{V}_{total}$ is the total velocity on the panel surface, and $\mathbf{V}_{ref}$ is the reference velocity. The calculated pressure distribution is integrated over the airframe surfaces to obtain the aerodynamic forces and moments acting on the fuselage. This procedure is used to evaluate the effect of the leading-aircraft wake on the fuselage surface pressure distribution and pitching moment response of the following aircraft under wake encounters. Although the NVLM incorporates airfoil lookup tables and a circulation-strength correction to account for the nonlinear aerodynamic characteristics, the underlying NVLM and source–doublet panel formulations are based on potential-flow theory. Therefore, viscous and turbulent flow phenomena in the surrounding flow field are not directly resolved.

2.2 Vortex particle method

In the considered wake encounter problem, the wake generated by the leading aircraft must be predicted over a long downstream distance until it reaches the rotor disks and airframe surfaces of the following aircraft. During forward flight, the rotor wake is convected, skewed, and deformed while interacting with other rotor wakes and surrounding airframe surfaces. Therefore, the wake model must be able to represent downstream transport and interaction of shed vorticity without imposing a specific wake geometry. VPM satisfies this requirement by representing the shed rotor wake as discrete Lagrangian vortex particles carrying vortex particle strength. The

particle positions are updated using the local velocity field, allowing the wake generated by multiple rotors to evolve freely as it convects downstream. This formulation is particularly advantageous for UAM wake encounter analysis because it can represent complex wake deformation and interaction without maintaining a connected vortex filament structure [34]. In grid-based CFD simulations, preserving coherent vortex structures over long downstream distances generally requires fine grid resolutions to constrain numerical dissipation. By contrast, VPM transports the wake vorticity directly through Lagrangian particles, enabling efficient prediction of the relative position of the wake and velocity disturbance imposed on the following aircraft. Consequently, VPM is used to simulate downstream wake evolution of the leading UAM aircraft and its interaction with the rotors and airframe surfaces of the following aircraft.

In VPM, the wake vorticity field is represented by S Lagrangian vortex particles as

$$\boldsymbol{\omega}(\mathbf{x},t)=\sum_{i=1}^{S}\xi_{\sigma}\left(\mathbf{x}-\mathbf{x}_{i}\right)\boldsymbol{\alpha}_{i} \tag{7}$$

where $\mathbf{x}_i$ is the position of the i-th vortex particle, $\boldsymbol{\alpha}_i$ is the vector-valued vortex particle strength within the particle, and ξ_σ is a regularization function with finite core size. This regularization function removes the singular behavior of the induced velocity when the distance between particles becomes small.

The velocity induced by vortex particles is calculated using the regularized Biot–Savart law. The velocity induced at the i-th particle by all other vortex particles is expressed as

$$\mathbf{u}\left(\mathbf{x}_{i},t\right)=-\sum_{j=1}^{S}\frac{1}{\sigma_{ij}^{3}}K(\rho)\left(\mathbf{x}_{i}-\mathbf{x}_{j}\right)\times\boldsymbol{\alpha}_{j} \tag{8}$$

$$\sigma_{ij}=\frac{1}{\sqrt{2}}\left(\sigma_{i}^{2}+\sigma_{j}^{2}\right)^{1/2} \tag{9}$$

$$\rho=\frac{\left|\mathbf{x}_{i}-\mathbf{x}_{j}\right|}{\sigma_{ij}} \tag{10}$$

$$K(\rho)=\frac{G(\rho)-\xi(\rho)}{\rho^{2}} \tag{11}$$

where σ_{ij} is the symmetric smoothing parameter between two particles, ρ is the nondimensional distance between particles, and $K(\rho)$ is the regularized Biot–Savart kernel.

The convection velocity of each vortex particle is defined as the sum of the freestream velocity, velocity induced by bound vortices on the rotor blades, velocity induced by airframe panels, and velocity induced by all other vortex particles:

$$\mathbf{V}_{conv} = \mathbf{V}_{\infty} + \mathbf{V}_{ind,bound} + \mathbf{V}_{ind,body} + \mathbf{V}_{ind,particle} \tag{12}$$

The particle position is then obtained by integrating the convection equation:

$$\frac{d\mathbf{x}_i}{dt} = \mathbf{V}_{conv}\left(\mathbf{x}_i, t\right) \tag{13}$$

In this study, the particle positions were updated using a second-order Runge–Kutta method. This temporal integration enables the resolution of the downstream convection and vertical displacement of the wake generated by the leading aircraft while determining the relative position of the convected wake with respect to the rotor disks and fuselage of the following aircraft. In addition, a slow-starting procedure was applied during the first rotor revolution to reduce the abrupt generation of strong initial starting vortices and improve numerical stability. Notably, the strength and core size of each vortex particle are kept constant during wake convection. This assumption represents a limitation of the proposed framework, as viscous diffusion and vortex stretching effects are not considered. This modeling assumption may not fully represent vortex-core spreading and the associated wake decay caused by viscous diffusion. In addition, because turbulence and instability-driven vortex breakdown are not explicitly represented, wake dispersion and the loss of vortex coherence in the downstream flow may be underrepresented. Consequently, the wake may remain more concentrated and coherent than in the physical flow, potentially leading to overprediction of the local induced velocity and the absolute magnitude of the wake-induced aerodynamic disturbance. The omission of vortex stretching may also limit the prediction of changes in vortex strength associated with wake deformation. Considering these limitations, the present results are interpreted primarily in terms of relative changes in wake convection and aerodynamic disturbance with advance ratio and vertical separation at the fixed streamwise separation.

3. Numerical validation

The aerodynamic prediction capability of the present solver has been assessed in previous studies through comparisons of rotor performance, blade loads, wake structures, and fuselage surface pressure distributions with experimental data, high-fidelity CFD results, or published numerical results. Therefore, the validation in this section mainly focuses on the wake-related quantities required for the wake encounter analysis between two full-configuration UAM aircraft. In the wake encounter problem, the aerodynamic response of the following UAM aircraft is governed by two wake-related quantities: local velocity disturbance induced by the rotor wake and downstream convection path of the wake structure generated by the leading aircraft. The former determines the

inflow distortion on the rotor disks and airframe surfaces of the following aircraft, whereas the latter reflects whether the convected wake intersects the following aircraft for a given relative position. Therefore, two validation cases are considered to assess the applicability of the proposed vortex-based solver to the wake encounter problem. The first examines the induced velocity field of a single rotor wake, which is directly related to the local inflow variations experienced by a following rotor or airframe surface. The second validates the tip-vortex trajectories of the ROBIN helicopter model at different advance ratios, providing a benchmark for assessing the capability of the solver to capture wake skewing, downstream convection, and wake structure distortion during forward flight. These two cases complement the previous aerodynamic validation of the solver by specifically assessing the magnitude of the wake-induced inflow disturbance and the downstream location of the wake, which determine the aerodynamic disturbance imposed on the following aircraft during wake encounter.

3.1 Validation of wake-induced velocity fields

Induced velocity measurements from the rotor experiment conducted by Heyson and Katzoff [26] are selected as the first validation case to verify whether the proposed solver can reproduce the inflow distortion generated by a rotor wake. The reference rotor consists of two untwisted and untapered rectangular blades with a radius of 7.5 ft (2.286 m) and NACA 0012 airfoil sections. The rotor has a solidity of 0.0543, hub offset of 30%, and shaft tilt angle of −9.2° (Table 2). To reproduce the experimental operating condition, a trim analysis is performed by prescribing a target thrust coefficient of 0.0032, while constraining pitching and rolling moment coefficients to zero. After obtaining the trim solution, the corresponding control angles are maintained constant during the unsteady simulation. The rotor operates at a tip speed of 500 ft/s (152.4 m/s) and an advance ratio of 0.095. Each blade is discretized using 15 chordwise and 25 spanwise panels. The simulation is run for 10 rotor revolutions with an azimuthal timestep of 5°. The operating and computational parameters for this validation are summarized in Table 3.

Table 2. Geometric properties of the Heyson and Katzoff rotor model.

Property	Value
Rotor radius, R [ft]	7.5
Solidity, σ [-]	0.0543
Hub offset [%]	30
Shaft tilt angle [°]	−9.2
Number of blades [-]	2
Airfoil [-]	NACA 0012

Table 3. Operating and numerical parameters for induced velocity validation.

Property	Value
Tip speed, ΩR [ft/s]	500
Advance ratio, μ [-]	0.095
Thrust coefficient, C_T [-]	0.0032
Number of grids [-] (Chordwise/Spanwise)	15/25
Azimuthal timestep [°]	5
Total revolutions [-]	10

Fig. 2 illustrates the sampling planes used to extract the induced velocity profiles for validation. The velocity field is sampled at two downstream locations, x/R = 2.07 and 3.14, measured from the rotor hub, where R denotes the rotor radius and the positive x-direction corresponds to downstream wake convection. The rotor plane is defined at z/R = 0, with positive and negative z-values corresponding to the upper and lower sides of the rotor plane, respectively. Fig. 3 compares the computed and measured profiles of the induced velocity ratio (v/v_0) at several vertical locations. Here, v denotes the local normal component of the induced-velocity measured along the sampling line; and v_0 is the reference average induced velocity based on momentum theory, used in the Heyson and Katzoff experiment to normalize the local induced velocity. Figs. 3(a)–(c) correspond to the near downstream plane at x/R = 2.07, whereas Figs. 3(d)–(f) pertain to the farther downstream plane at x/R = 3.14. Overall, the present results reproduce the measured trends of the induced velocity ratio on both the retreating and advancing sides, including the lateral locations (at which rapid velocity variations occur) and the overall magnitude of velocity perturbations. This agreement indicates that the solver accurately captures the primary inflow distortion produced by the rotor wake in the downstream region. The mean absolute error between the experimental data and the present results was calculated at the experimental measurement locations. Considering all measurement locations for the six profiles, the absolute error ranged from 0.003 to 3.478, with the minimum and maximum values both occurring in Fig. 3(e) at y/R = 0.477 and y/R = -1.000, respectively.

Nevertheless, local discrepancies are observed in several profiles. In particular, in Fig. 3(b), the induced velocity ratio is slightly overpredicted near the rotor center, whereas in Fig. 3(e), it is somewhat underpredicted on the retreating side. These differences may be attributed to the simplified rotor representation adopted in the simulations, with the hub and strut bar geometries excluded [35]. In the experiment, these structural components may have modified the local flow field near the rotor center, thereby altering the measured induced velocity distribution, whereas the present model primarily resolves the blade-bound circulation and wake vorticity shed

from the rotor blades. Despite these localized differences, the solver reasonably predicts both the spatial distribution and magnitude of the induced velocity ratio at both downstream planes. This confirms that the wake model can reproduce the downstream induced velocity field with sufficient accuracy for the present wake encounter analysis, in which the aerodynamic response of the following aircraft depends on the velocity disturbances convected from the leading-aircraft wake.

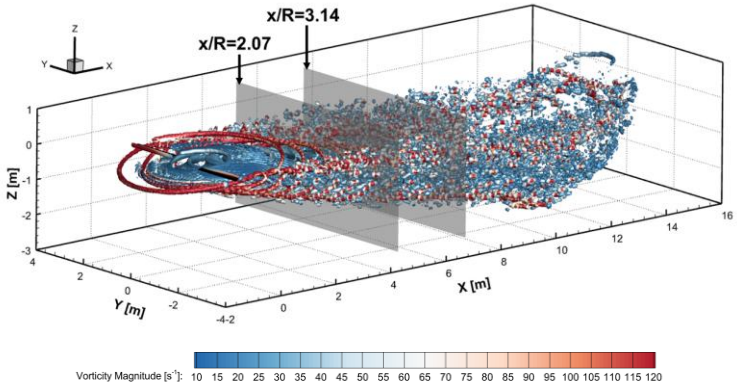

Fig. 2. Sampling planes for induced velocity validation at x/R = 2.07 and 3.14 downstream of the rotor.

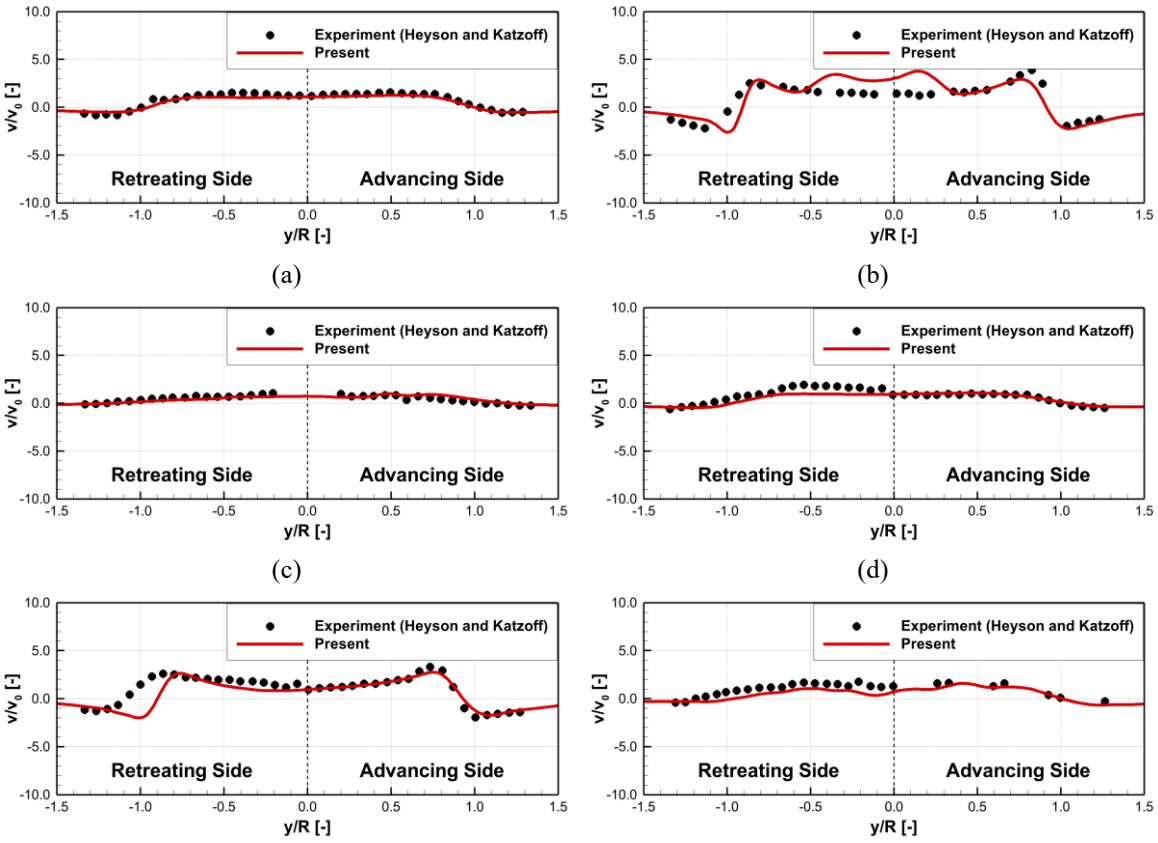

Fig. 3. Comparison of induced velocity ratio profiles between the experimental data and present results: (a)–(c) x/R = 2.07 and (d)–(f) x/R = 3.14; (a) z/R = 0.11, (b) z/R = −0.16, (c) z/R = −0.82, (d) z/R = 0.10, (e) z/R = −0.23, and (f) z/R = −0.63.

3.2 Validation of wake structures at different advance ratios

The second validation case assesses the capability of the solver to predict tip vortex trajectories in forward flight. Although the present study focuses on a multirotor UAM aircraft with a side-by-side rotor arrangement, the NASA ROBIN helicopter model provides a well-established benchmark for evaluating rotor wake convection and its interaction with the fuselage [27]. As the advance ratio changes, the balance between freestream convection and rotor-induced downwash varies, altering the wake trajectory and positions of tip vortices downstream of the rotor. Therefore, the tip vortex trajectory under different advance ratios must be reliably predicted before applying the solver to the leader–follower UAM configurations considered in the following sections. As shown in Fig. 4, the configuration consists of a single main rotor and fuselage. The main rotor has four rectangular blades with a radius of 0.86 m, an aspect ratio of 12.98, and NACA 0012 airfoil sections. The blade geometry includes a coning angle of 1.5°, linear twist of −8°, hub offset of 24%, and shaft tilt angle of −3°. The fuselage length is 1.72 m, approximately two times the rotor radius. The geometric properties of the ROBIN helicopter model are summarized in Table 4.

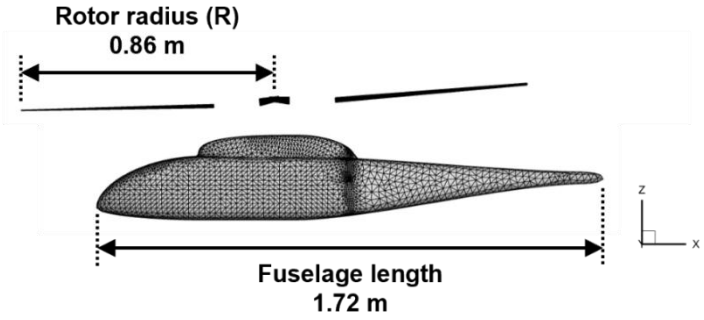

Fig. 4. Geometry and surface discretization of the ROBIN helicopter model used for tip vortex trajectory validation.

Table 4. Geometric properties of the ROBIN helicopter model.

Property	Value
Rotor radius, R [m]	0.86
Fuselage length [m]	1.72
Aspect ratio [-]	12.98
Hub offset [%]	24
Coning angle [°]	1.5
Twist angle [°]	−8 (linear)
Shaft tilt angle [°]	−3
Number of blades [-]	4
Airfoil [-]	NACA 0012

Table 5. Operating and numerical parameters for tip vortex trajectory validation.

Property	Value
Advance ratio, μ [-]	0.15, 0.23
Rotational speed [rpm]	2111.4
Thrust coefficient, C_T [-]	0.0064
Pitching moment coefficient [-]	0
Rolling moment coefficient [-]	0
Number of blade grids [-] (Chordwise/Spanwise)	15/25
Number of fuselage grids [-]	8286
Azimuthal timestep [°]	5
Total revolution [-]	8

Table 6. Trim control angles for the ROBIN helicopter model at two advance ratios.

Case	Advance ratio, μ [-]	θ_0 [°]	θ_{1c} [°]	θ_{1s} [°]
Experiment	0.15	6.55	−1.39	1.99
	0.23	6.47	−1.07	3.23
Present	0.15	6.67	2.03	−0.19
	0.23	6.29	1.52	−0.39

For the tip vortex trajectory validation, the rotor trim state is first established for each advance ratio because the wake geometry is strongly affected by blade loading and control inputs. Validation is performed at μ = 0.15 and 0.23 with a fixed rotor speed of 2111.4 rpm, and the thrust coefficient is set as 0.0064 for both cases. The pitching and rolling moment coefficients are constrained to zero to ensure consistency with the force and moment balances used in the reference experiment. The rotor blades are modeled using the NVLM with 15 chordwise and 25 spanwise lattice panels, while the fuselage surface is represented by 8286 triangular panels using the source–doublet panel method. This combined rotor and fuselage representation accounts for the influence of the airframe on the near-wake development and subsequent tip vortex convection. Unsteady simulations are performed for eight rotor revolutions with an azimuthal timestep of 5°. The operating and numerical parameters are summarized in Table 5.

Notably, in the experiment, the rotor was trimmed to obtain a zero flapping response, which requires resolving blade dynamics [36]. As the present solver does not incorporate blade flapping motion, the lateral and longitudinal flap angles are prescribed as zero, and the cyclic pitch components are adjusted to satisfy the zero hub moment condition. The resulting trim control angles, including collective pitch angle θ_0, lateral cyclic pitch angle θ_{1c}, and

longitudinal cyclic pitch angle θ_{1s}, are compared with the experimental values in Table 6. These trim controls are held fixed during the unsteady simulations for comparing the tip vortex trajectories.

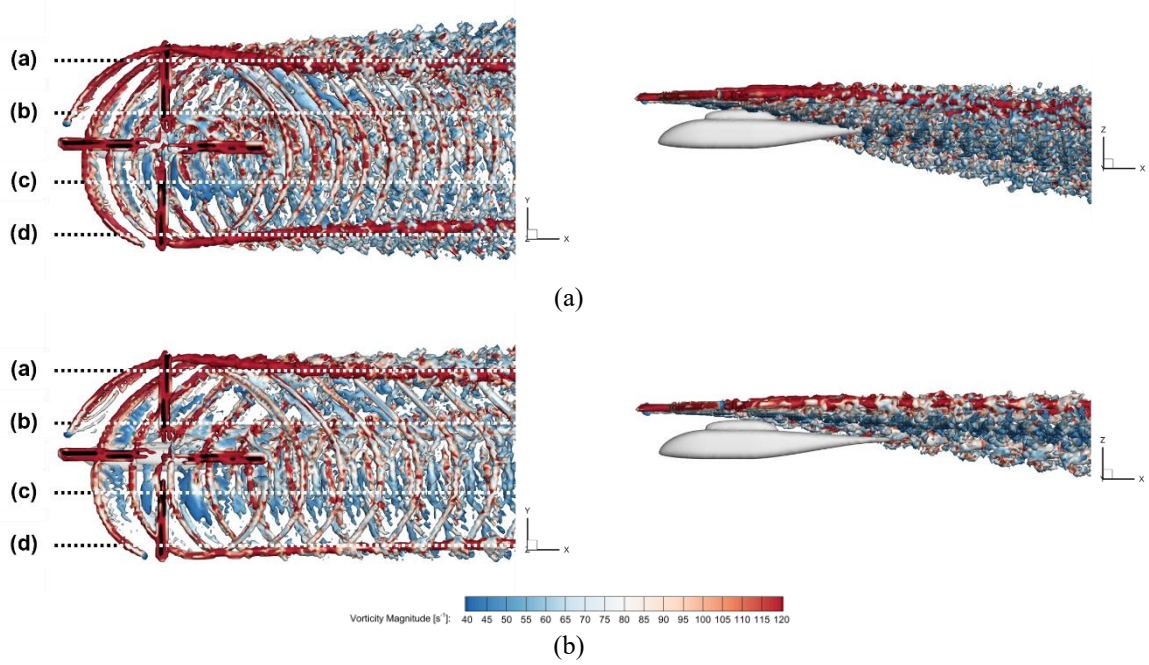

Fig. 5. Wake structures of the ROBIN helicopter model visualized using Q-criterion iso-surfaces colored by vorticity magnitude with top view (left) and side view (right): (a) μ = 0.15 and (b) μ = 0.23; dashed lines indicate the lateral stations for tip vortex trajectory evaluation.

Fig. 5 shows the predicted wake structures of the ROBIN helicopter model at μ = 0.15 and 0.23. The wake is visualized using Q-criterion iso-surfaces colored by vorticity magnitude, and both top and side views are presented to illustrate the lateral spreading and vertical convection of the rotor wake. During forward flight, the tip vortices shed from the blade tips are convected downstream by the freestream while being displaced downward by the rotor-induced velocity field. Therefore, the wake geometry is governed by the relative magnitudes of freestream convection and induced downwash [37]. As the advance ratio increases, the streamwise convection of the helical wake per rotor revolution increases relative to its vertical descent, producing increased streamwise spacing between successive tip vortices and a larger wake skew angle. Here, the wake skew angle is defined as the angle between the rotor disk normal and the wake centerline or wake boundary. As evidenced in Fig. 5, the wake at μ = 0.23 is convected farther downstream than that at μ = 0.15. Additionally, the side views show that the wake remains closer to the rotor plane at the higher advance ratio, whereas the lower advance ratio produces a more pronounced downward displacement below the rotor disk. The dashed lines in Fig. 5 indicate the lateral stations used for the tip vortex trajectory comparison, corresponding to y/R = 0.8, 0.3, −0.3, and −0.8. At these stations,

the tip vortex trajectories over the last quarter revolution are extracted and compared with the experimental measurements and numerical results reported by Kenyon and Brown [38].

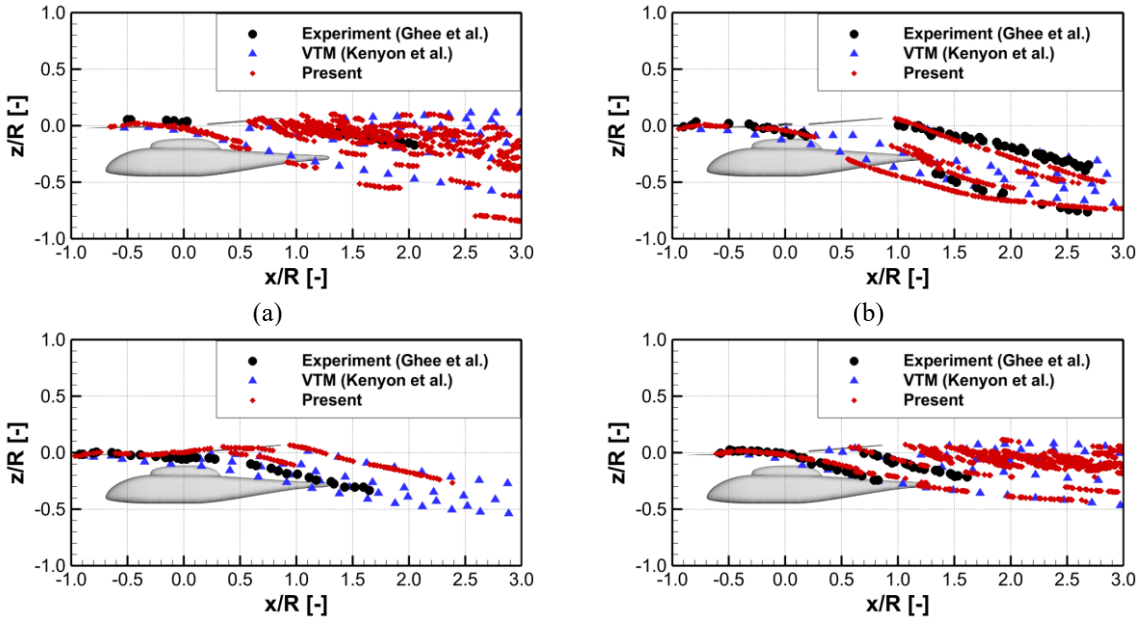

Fig. 6. Comparison of tip vortex trajectories among the experimental measurements, VTM results of Kenyon et al. [27], and the present result at $\mu = 0.15$: (a) $y/R = 0.8$, (b) $y/R = 0.3$, (c) $y/R = -0.3$, and (d) $y/R = -0.8$.

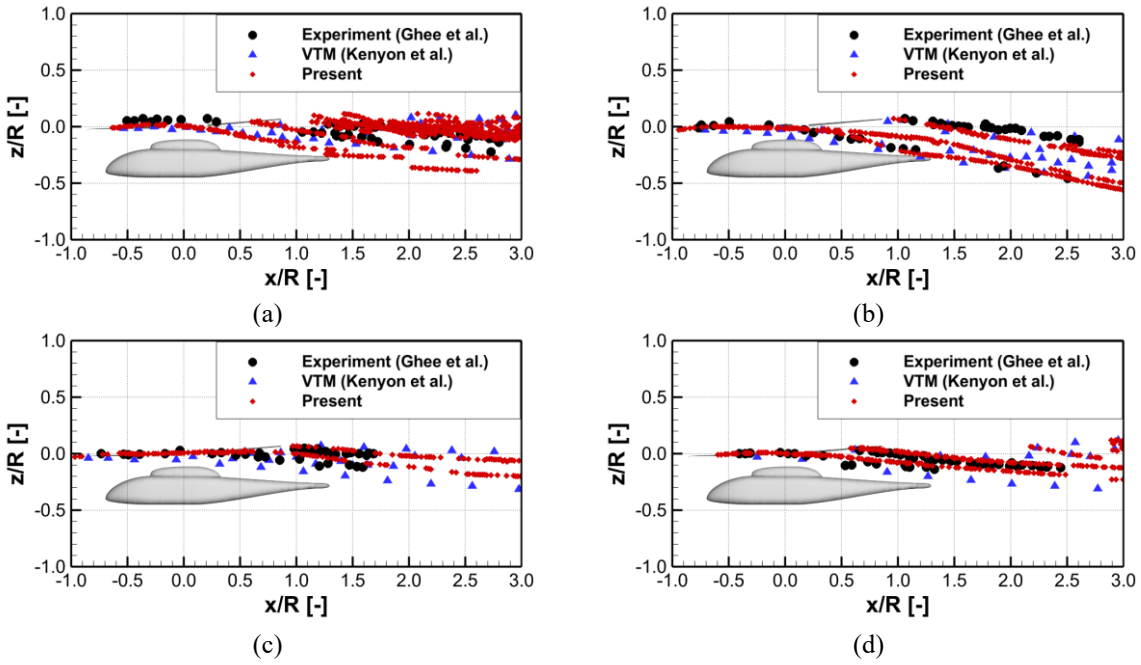

Fig. 7. Comparison of tip vortex trajectories among the experimental measurements, VTM results of Kenyon et al. [27,38], and the present result at $\mu = 0.23$: (a) $y/R = 0.8$, (b) $y/R = 0.3$, (c) $y/R = -0.3$, and (d) $y/R = -0.8$.

Figs. 6 and 7 compare the predicted tip vortex trajectories with the experimental measurements and vortex transport method results at μ = 0.15 and 0.23, respectively. Overall, the proposed method reproduces the main features of the measured tip vortex trajectories at both advance ratios. The solver captures the downstream progression of the tip vortices and change in vertical displacement across the lateral stations, indicating that the variation in wake trajectory with advance ratio is reasonably predicted. However, several local discrepancies are observed, particularly at the outer lateral stations. For example, at y/R = 0.8 in Fig. 6(a), the proposed method predicts a slightly lower tip vortex trajectory than the experimental measurements. This difference may be related to the simplified vortex treatment adopted in the present analysis: the vortex particles are convected without explicit viscous diffusion, and their strengths are maintained constant during the wake simulation. Consequently, the induced velocity of the tip vortices may be preserved more strongly in the downstream region, leading to a slightly larger downward displacement of the predicted trajectories. Additional differences may arise from the aerodynamic trim treatment, because the proposed solver does not directly resolve the blade flapping dynamics used in the experimental trim condition. Despite these limitations, the predicted trajectories show reasonable agreement with the reference experiment and numerical results in terms of the wake convection path and advance ratio dependence. This validation confirms that the proposed solver can predict the primary rotor wake structure and tip vortex trajectory under forward flight conditions. Although the validation is based on a single-rotor helicopter configuration, it supports the use of the present method for assessing the wake trajectory and encounter location in the full-configuration UAM simulations considered in the following sections.

4. Problem definition and numerical setup

4.1 Full-configuration UAM aircraft model

In this study, the NASA side-by-side UAM aircraft in full configuration was considered, and its geometric definition is publicly available as an OpenVSP model [39]. In the present numerical model, the landing gear and strakes are omitted to reduce geometric complexity, whereas the main aerodynamic components are retained, including the two main rotors, rotor cowlings, lateral support structures, fuselage, and inverted V-tail (Fig. 8). The two main rotors are mounted laterally on both sides of the fuselage, forming an intermeshing side-by-side arrangement with a rotor overlap ratio of 15%. As indicated in the top view of Fig. 8, the left rotor rotates clockwise and the right rotor rotates counterclockwise when viewed from above. This counter-rotation arrangement and the overlapping disk region are important geometric features because they determine the initial wake orientation, interaction between the two rotor wakes, and wake loading on the surrounding airframe surfaces.

Each rotor comprises four blades with a radius of 3.203 m. The blade chord decreases from 0.217 m at the root to 0.130 m near the tip, and a swept and tapered tip with a sweep angle of 15° is applied in the outer blade region. The blades have a coning angle of 3.1°, linear twist of −16°, and shaft tilt angle of −3°. The hub offset is 16%, and the fuselage length is 9.144 m. Two airfoils are assigned along the span: Boeing VR-12 is used for the inner blade region ($r/R < 0.85$), and Sikorsky SSC-A09 is used for the outer blade region ($r/R > 0.95$). The blade sections between these radial locations are generated by linear interpolation. The main geometric properties of the full-configuration side-by-side UAM aircraft are summarized in Table 7.

Table 7. Geometric properties of the full-configuration side-by-side UAM aircraft.

Property	Value
Rotor radius, R [m]	3.203
Chord length, c [m]	0.217 (root), 0.130 (tip)
Tip sweep angle [°]	15 (linear)
Fuselage length [m]	9.144
Rotor overlap ratio [%]	15
Hub offset [%]	16
Coning angle [°]	3.1
Twist angle [°]	−16 (linear)
Shaft tilt angle [°]	−3
Number of rotors [-]	2
Number of blades per rotor [-]	4
Airfoil section [-]	VR-12 ($r/R < 0.85$) SSC-A09 ($r/R > 0.95$)

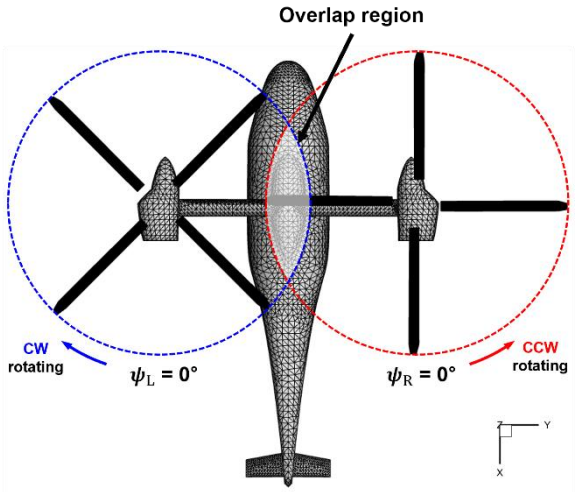

(a)

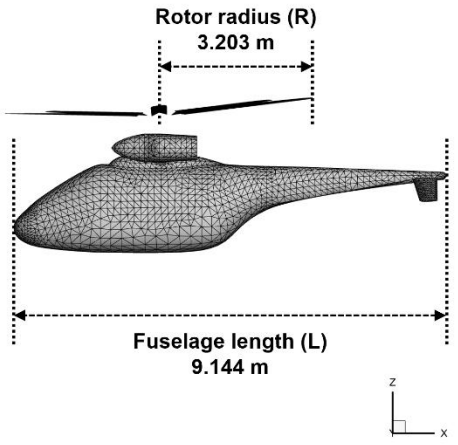

(b)

Fig. 8. Discretized geometry of the full-configuration side-by-side UAM aircraft: (a) top and (b) side views.

4.2 Simulation conditions for wake encounter analysis

The operating and numerical parameters applied to each UAM aircraft in the wake encounter simulations are lied in Table 8. Two advance ratios, μ = 0.15 and 0.23, were considered to examine wake encounter characteristics under different forward-flight speeds. These advance ratios were selected to match those used in the ROBIN helicopter tip vortex trajectory validation in Section 3.2, thereby maintaining consistency between the wake trajectory validation and the full-configuration UAM wake encounter simulations. Except for the advance ratio, all operating conditions were kept identical across cases to ensure that changes in the aerodynamic response of the following aircraft could be attributed solely to the wake encounter effect rather than to variations in rotor operating conditions. The rotor speed was fixed at 491 rpm, and the unsteady simulations were conducted for 12 rotor revolutions. The convergence of the following-aircraft response was assessed using the revolution-averaged thrust. The relative difference in mean thrust between the last two revolutions was less than 0.15% for all six cases, indicating that the mean rotor response had reached a stable level. In the numerical discretization, the rotor blades were modeled using quadrilateral vortex lattice elements for NVLM. By contrast, the fuselage, cowlings, and tail surfaces were represented by triangular panels in the source–doublet panel method. The azimuthal timestep and blade grid resolution were selected based on numerical sensitivity assessments. Azimuthal timesteps of 10°, 5°, and 3° were examined using a fixed blade discretization of 22/30 panels, while blade discretization of 12/20, 22/30, and 32/40 panels in the chordwise/spanwise directions were examined using a fixed timestep of 5°. Refining the timestep from 5° to 3° changed the mean thrust by 0.40%, while increasing the blade discretization from 22/30 to 32/40 panels resulted in a difference of 0.80%. Considering both numerical sensitivity and computational cost, a timestep of 5° and a blade discretization of 22 chordwise and 30 spanwise panels were adopted. The airframe surfaces were discretized using 9188 triangular panels. For the wake analysis, three near-wake panels were used downstream of the blade trailing edge, and the vortex core radius was set to 0.2 times the blade chord length.

Table 8. Operating and numerical parameters applied to each UAM aircraft in wake encounter simulations.

Property	Value
Advance ratio, μ [-]	0.15, 0.23
Rotational speed [rpm]	491
Gross weight, W [kg]	1792

Pitching moment [Nm]	0
Rolling moment [Nm]	0
Number of blade grids [-] (Chordwise/Spanwise)	22/30
Number of fuselage grids [-]	9188
Number of near-wake panels [-]	3
Vortex core radius, r_c/c [-]	0.2
Azimuthal timestep [°]	5
Total revolutions [-]	12

For the wake encounter simulations, a baseline trim analysis was first performed for a single UAM aircraft in full configuration, rather than for the two-aircraft leader–follower configuration. The collective, lateral cyclic, and longitudinal cyclic pitch angles were adjusted such that the target total thrust equaled the aircraft weight corresponding to a gross mass of 1792 kg, while the target pitching and rolling moments were constrained to zero [40]. Moreover, the shaft tilt angle of both rotors was set to $-3°$, following the experimental condition used by Wright and Cummings [41], to maintain the identical aircraft attitude across all wake encounter cases. Because the port and starboard rotors rotate in opposite directions and experience different local inflow environments owing to the side-by-side arrangement and fuselage interference, trim control angles were determined separately for each rotor. The resulting trim controls were then imposed in the unsteady wake encounter simulations. No additional trim adjustment was applied to the following aircraft once it entered the disturbed wake of the leading aircraft. This fixed-control treatment helps evaluate the direct aerodynamic effect of the incoming wake on the following aircraft. The trim control angles obtained at μ = 0.15 and 0.23 are summarized in Tables 9 and 10, respectively.

Table 9. Trim control angles of the starboard and port side rotors of the side-by-side UAM aircraft at μ = 0.15.

Advance ratio, μ [-]	Rotor side [-]	θ_0 [°]	θ_{1c} [°]	θ_{1s} [°]
0.15	Starboard side	7.83	3.69	−3.69
	Port side	7.58	2.93	−1.60

Table 10. Trim control angles of the starboard and port side rotors of the side-by-side UAM aircraft at μ = 0.23.

Advance ratio, μ [-]	Rotor side [-]	θ_0 [°]	θ_{1c} [°]	θ_{1s} [°]
0.23	Starboard side	7.94	3.37	−5.31
	Port side	7.48	3.04	−2.67

Moreover, a simulation matrix is constructed to examine the effects of advance ratio and vertical separation distance on wake encounter between two full-configuration side-by-side UAM aircraft. Fig. 9 shows the relative locations of the leading and following aircraft, and Table 11 summarizes the corresponding cases. The coordinate system is defined as follows: the x-axis is aligned with the freestream and downstream wake convection direction, the y-axis corresponds to the lateral direction across the side-by-side rotors, and the z-axis is defined as the vertical direction (positive upward). The position of the following aircraft is specified relative to that of the leading aircraft using nondimensional separations normalized by the rotor radius R. In all cases, the following aircraft is placed behind the leading aircraft at a fixed streamwise separation of $x/R = 6$, corresponding to three rotor diameters. This separation is selected to represent a close trail condition, where the wake generated by the leading aircraft has developed downstream and reaches the following aircraft. This distance is consistent with the upper bound of the fixed trail formation spacing of 1–3 rotor diameters, specified in the U.S. Air Force helicopter operation manual [42]. By fixing the streamwise separation, the effects of advance ratio and vertical offset can be compared at the same downstream location. Therefore, the dependence of wake evolution and the aerodynamic response of the following aircraft on streamwise separation is outside the scope of the present study and remains a limitation of the current analysis.

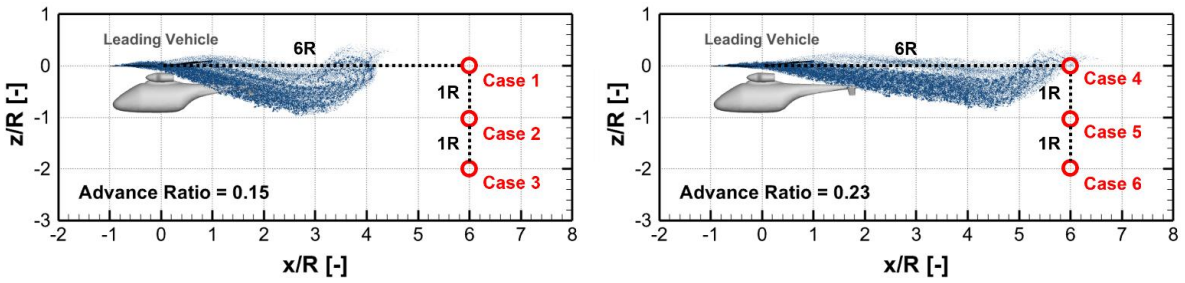

(a) (b)

Fig. 9. Wake encounter case definition for the side-by-side UAM aircraft at two advance ratios and three vertical separation distances with a fixed streamwise separation of $x/R = 6$: (a) $\mu = 0.15$ and (b) $\mu = 0.23$.

Table 11. Wake encounter cases defined by the advance ratio and separation distance.

Case	Advance ratio, μ [-]	Streamwise separation, x/R [-]	Vertical separation, z/R [-]
1	0.15	6	0
2			−1
3			−2
4	0.23	6	0
5			−1
6			−2

Two advance ratios, $\mu = 0.15$ (Cases 1–3) and 0.23 (Cases 4–6), are considered to represent different forward-flight speeds and corresponding skewed wake structures. For each advance ratio, the following aircraft is located at three vertical-separation distances of $z/R = 0$, -1, and -2 relative to the leading aircraft. Here, $z/R = 0$ denotes the same altitude condition, whereas negative values indicate that the following aircraft is located below the leading aircraft. The vertical separation is examined because the advance ratio governs the wake skew angle and convection path of the leading aircraft wake, whereas the vertical offset determines which regions of the following aircraft are exposed to the convected wake, including rotor disk ingestion and wake impingement on the fuselage and tail surfaces. The six cases are thus designed to systematically assess the effects of the leading-aircraft wake development and relative vertical position of the following aircraft on the rotor loads, fuselage pressure distribution, and aerodynamic moments of the following aircraft.

5. Results and discussion

5.1 Wake structures and encounter characteristics

The wake structures are first examined to elucidate the encounter characteristics between the leading and following aircraft under different advance ratios and vertical separation distances. Fig. 10 shows the wake structures of the leading and following aircraft (blue and red particles, respectively). The left and right columns correspond to $\mu = 0.15$ and 0.23, respectively, while the rows (from top to bottom) correspond to $z/R = 0$, -1, and -2. This layout enables direct comparison of the advance ratio effects at a fixed vertical separation and vertical-separation effects at a fixed advance ratio.

For the same vertical location cases shown in Figs. 10(a) and 10(b), the wake generated by the leading aircraft reaches the region occupied by the following aircraft at both advance ratios. At $\mu = 0.15$, the lower freestream velocity results in a smaller wake skew angle and stronger relative contribution of induced downwash, causing the wake to descend more notably toward the following aircraft. Consequently, the leading-aircraft wake overlaps extensively with the rotor and fuselage region of the following aircraft. At $\mu = 0.23$, the larger freestream velocity increases the wake skew angle and transports the tip vortex system farther downstream with reduced vertical descent over the same streamwise distance. Thus, the encounter region shifts relative to the following aircraft, even though both aircraft remain at the same altitude. This indicates that the wake encounter pattern is determined not only by the geometric separation but also by the wake trajectory controlled by the advance ratio. The effect of vertical separation becomes more evident when the following aircraft is positioned below the leading aircraft. At

$z/R = -1$, the leading aircraft wake still reaches the upper region of the following aircraft at $\mu = 0.15$ (Fig. 10(c)), although the wake encounter region is contracted compared with that in the same-altitude case. In other words, the lower-speed condition maintains a substantial wake influence even when the following aircraft is vertically displaced (below the leader). By contrast, at $\mu = 0.23$ (Fig. 10(d)), the wake remains closer to the rotor disk, and the following aircraft is positioned farther below the main wake region, leading to a weaker direct encounter. For $z/R = -2$, the separation between the leading aircraft wake and following aircraft becomes more pronounced. As shown in Fig. 10(e), the wake at $\mu = 0.15$ still exhibits downward development and partially approaches the upper region of the following aircraft. However, the overlap with the main wake region is substantially reduced compared with the smaller vertical-separation cases at the same advance ratio. In Fig. 10(f), at $\mu = 0.23$, the wake passes primarily above the following aircraft, and the wake systems of the two aircraft are more clearly separated without wake interaction. Therefore, Case 6 ($\mu = 0.23$; $z/R = -2$) is expected to correspond to the weakest wake encounter condition because the leading aircraft wake passes mostly above the following aircraft. Conversely, Cases 1 and 4 ($z/R = 0$) are expected to impose the strongest wake disturbance because the following aircraft is directly exposed to the convected wake of the leading aircraft.

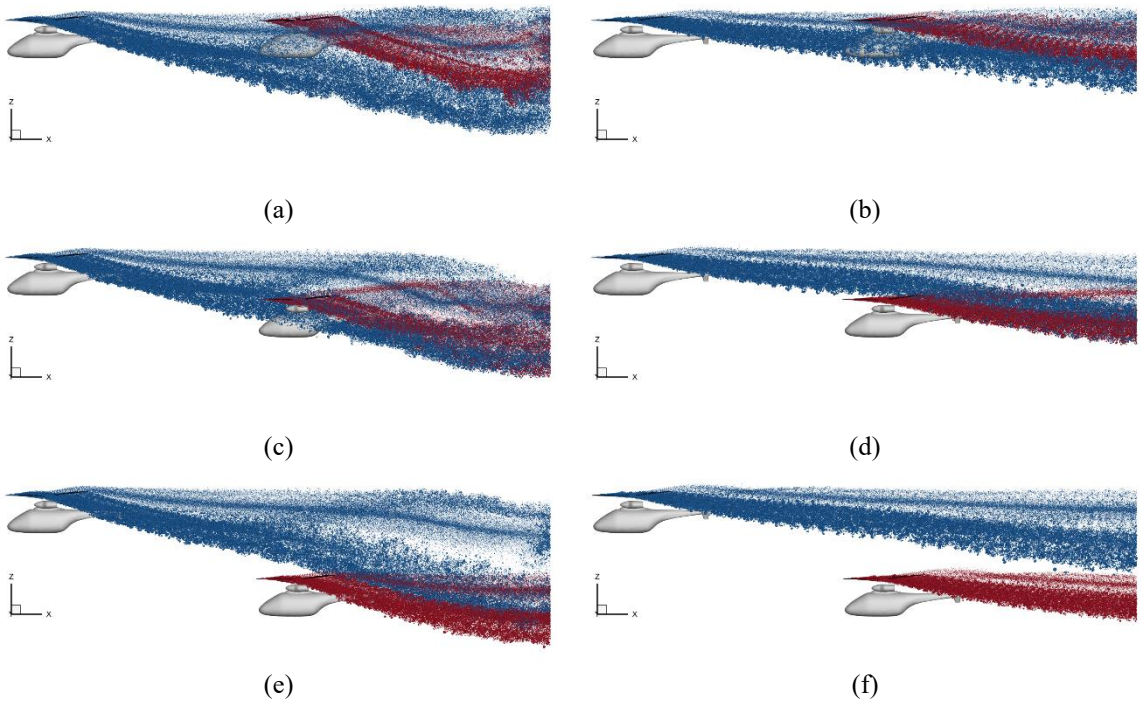

Fig. 10. Wake structures of the leading and following aircraft for different advance ratios and vertical separation distances in forward flight, with the left and right columns corresponding to $\mu = 0.15$ and 0.23, respectively, and the rows corresponding to $z/R = 0$, -1, and -2 from top to bottom: (a) Case 1, (b) Case 4, (c) Case 2, (d) Case 5, (e) Case 3, and (f) Case 6.

Overall, the wake encounter pattern is governed by the combined effects of advance ratio and vertical separation distance. At the lower advance ratio, the leading aircraft wake exhibits larger downward displacement, allowing wake effects on the following aircraft to persist even when the following aircraft is positioned below the leading aircraft. At the higher advance ratio, stronger streamwise convection causes the wake structure to pass farther downstream and reduces direct wake exposure of the following aircraft as the vertical separation increases. These differences in wake trajectory and encounter location constitute the physical basis for the variations in rotor thrust and torque, fuselage pressure distribution, and aerodynamic moment response, as discussed in the following sections.

5.2 Rotor thrust and torque response of the following aircraft

Rotor thrust histories are examined to quantify the aerodynamic effects of wake encounter on the following aircraft. As shown in Fig. 10, the wake generated by the leading aircraft reaches the rotor disks of the following aircraft with encounter patterns governed by the advance ratio and vertical separation distance. These patterns alter the local inflow over the following rotors and produce unsteady variations in thrust. Fig. 11 compares the total rotor thrust histories of the leading and following aircraft over 12 rotor revolutions. Figs 11(a) and 11(b) correspond to Cases 1–3 (μ = 0.15) and Cases 4–6 (μ = 0.23), respectively. For both advance ratios, the leading aircraft (undisturbed by upstream-aircraft wake) maintains a nearly periodic thrust level with minimal variation across cases. By contrast, the following aircraft exhibits pronounced thrust reduction and increased unsteadiness after the leading aircraft wake enters its rotor disk region.

At μ = 0.15, Case 1 exhibits a temporary increase in thrust before the main wake encounter, followed by a rapid decrease as the main wake is ingested by the following rotors. As the vertical separation increases, wake exposure and thrust loss decrease, although some wake influence remains in Case 3 because of the larger downward displacement of the wake at the lower advance ratio. At μ = 0.23, the thrust decrease in Case 4 occurs earlier than that in Case 1 because of the stronger streamwise wake convection. The wake influence is progressively reduced in Cases 5 and 6 as the vertical separation increases, and the thrust in Case 6 approaches most closely that of the leading aircraft because the main wake passes above the following rotor disks (Fig. 10(f)).

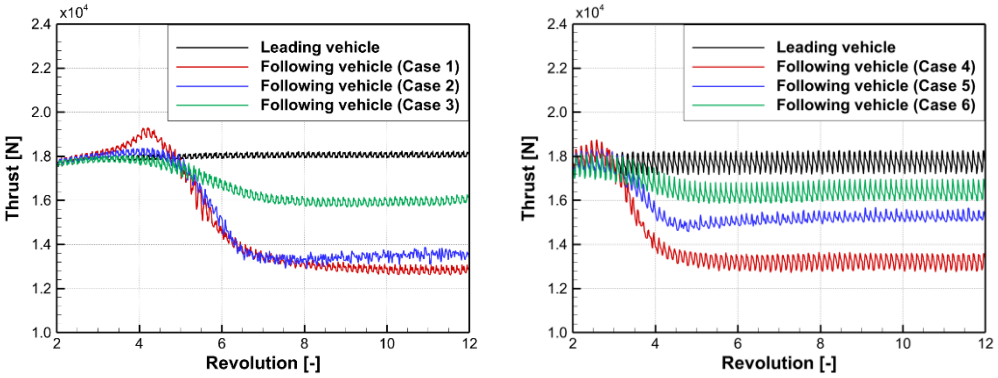

Fig. 11. Comparison of thrust histories between the leading and following UAM aircraft for different advance ratios: (a) $\mu = 0.15$ and (b) $\mu = 0.23$.

Fig. 12 compares thrust distributions on the starboard rotors during the last rotor revolution to clarify the local loading mechanism responsible for the thrust histories shown in Fig. 11. The left and right columns correspond to $\mu = 0.15$ and 0.23, respectively. Fig. 12(a) shows the starboard rotor of the leading aircraft, whereas Figs. 12(b)–(d) correspond to the starboard rotor of the following aircraft at $z/R = 0$, -1, and -2, respectively. The leading rotor exhibits a nearly repeatable thrust distribution at both advance ratios. Under the same-altitude condition (Fig. 12(b)), a broad low-thrust region appears on the following rotor at both advance ratios. This loading deficit is consistent with the wake structures in Figs. 10(a) and 10(b), where the wake of the leading aircraft is ingested by the rotor disk of the following aircraft. Pronounced thrust reduction occurs over the azimuthal sector of approximately 135°–180°, where the following rotor encounters the concentrated vorticity shed from the leading aircraft. The wake-induced velocity in this sector modifies the effective inflow angle of the blade elements and reduces the local aerodynamic loading. The vertical-separation cases in Figs. 12(c) and 12(d) demonstrate the recovery of the rotor loading as the following aircraft is displaced below the leading aircraft. At $z/R = -1$, the following rotor at $\mu = 0.15$ still experiences substantial load distortion because the leading aircraft wake descends toward the upper portion of the following aircraft. The distribution exhibits high loading deficit regions, reflecting the unsteady inflow imposed by the interacting rotor wakes of the leading aircraft. In contrast, at $\mu = 0.23$, the low-thrust region contracts, and the loading pattern approaches that of the leading rotor as the convected wake remains farther above the following rotor disk. At $z/R = -2$, the thrust distribution further recovers for both advance ratios. Case 3 (Fig. 12(d), left) still retains a localized loading deficit owing to the downward displacement of the wake at the lower advance ratio, whereas Case 6 (Fig. 12(d), right) shows the closest agreement with the leading rotor distribution because the leading aircraft wake passes mostly above the following rotor.

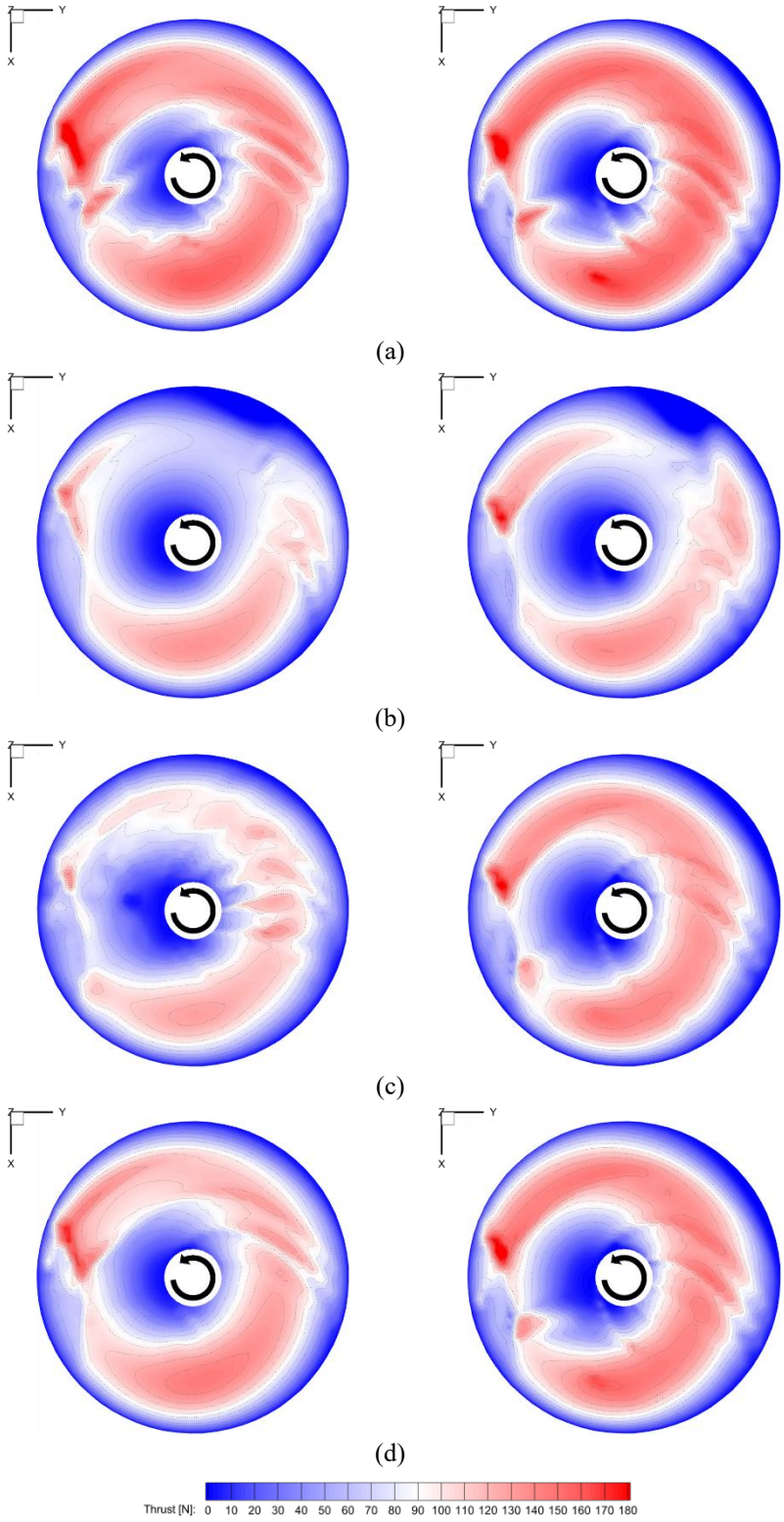

Fig. 12. Thrust distributions on the starboard side rotors of the leading and following aircraft during the last rotor revolution. The left and right columns correspond to $\mu = 0.15$ and 0.23, respectively: (a) leading rotor, (b) following rotor at $z/R = 0$, (c) following rotor at $z/R = -1$, and (d) following rotor at $z/R = -2$.

The mean rotor loads were further examined to evaluate the aerodynamic performance degradation of the following aircraft during wake encounter. Tables 12 and 13 summarize the mean thrust and total rotor torque over the last rotor revolution, along with their reductions relative to the corresponding values of the leading aircraft. The thrust reduction is defined as the percentage decrease in the mean thrust of the following aircraft. Because the port and starboard rotors of the side-by-side UAM aircraft rotate in opposite directions, the total rotor torque is evaluated as the sum of the absolute mean torques of the two rotors to avoid cancellation. The torque reduction is then defined as the percentage decrease in this total rotor torque relative to that of the leading aircraft.

Table 12 reveals that the mean thrust of the following aircraft is substantially reduced under wake encounter effects, and this reduction decreases with increasing vertical separation. At $\mu = 0.15$, the thrust reduction decreases from 29.12% at $z/R = 0$ (Case 1) to 25.17% at $z/R = -1$ (Case 2) and 11.10% at $z/R = -2$ (Case 3). At $\mu = 0.23$, the reduction decreases from 25.63% at $z/R = 0$ (Case 4) to 14.17% at $z/R = -1$ (Case 5) and 7.70% at $z/R = -2$ (Case 6). These results indicate that the mean thrust loss is primarily governed by the degree of wake ingestion into the rotor disks of the following aircraft. When both aircraft are at the same altitude, the convected wake overlaps extensively with the rotor disk region, producing the largest thrust degradation. As the following aircraft is displaced downward, this overlap is reduced, and the rotor thrust partially recovers. The smallest thrust reduction occurs in Case 6, consistent with the wake structure in Fig. 10(f), where the leading aircraft wake passes mostly above the following aircraft.

The torque response in Table 13 exhibits a weaker and less monotonic variation compared to the thrust response. The torque reductions are smaller than thrust reductions for all cases, indicating that wake encounter affects the mean thrust more strongly than the mean total rotor torque. At $\mu = 0.15$, torque reduction increases from 4.50% in Case 1 to 8.02% in Case 2, before decreasing to 1.34% in Case 3. This nonmonotonic behavior indicates that the torque response is not determined solely by the vertical separation distance or overall wake overlap; instead, it is sensitive to the local inflow distribution over the rotor disk, which influences the sectional angle of attack and tangential blade loading. At $\mu = 0.23$, the torque reduction decreases more systematically from 5.15% in Case 4 to 2.84% in Case 5 and 1.09% in Case 6, reflecting diminished wake effects on the following rotors with increasing vertical separation.

Fig. 13 summarizes the mean rotor load variations in normalized form using the corresponding values of the leading aircraft at each advance ratio as reference values. The normalized thrust generally recovers with increasing vertical separation, whereas the torque exhibits smaller variations and a nonmonotonic case dependence at $\mu = 0.15$. This difference arises because the mean thrust primarily reflects wake ingestion into the rotor disks, whereas

the total rotor torque is also sensitive to local changes in sectional blade loading caused by nonuniform inflow.

Table 12. Mean thrust and thrust reduction of the leading and following UAM aircraft.

Case	Leading vehicle [N]	Following vehicle [N]	Thrust reduction [%]
1		12,832	29.12 ▼
2	18,103	13,547	25.17 ▼
3		16,093	11.10 ▼
4		13,213	25.63 ▼
5	17,766	15,249	14.17 ▼
6		16,398	7.70 ▼

Table 13. Mean torque and torque reduction of the leading and following UAM aircraft.

Case	Leading vehicle [Nm]	Following vehicle [Nm]	Torque reduction [%]
1		2989	4.50 ▼
2	3130	2879	8.02 ▼
3		3088	1.34 ▼
4		2872	5.15 ▼
5	3028	2942	2.84 ▼
6		2995	1.09 ▼

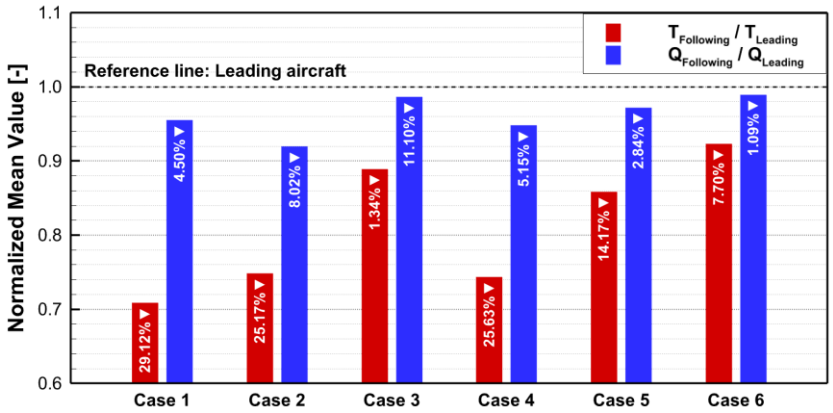

Fig. 13. Mean thrust and torque of the following aircraft normalized by the corresponding values of the leading aircraft for each wake encounter case. Bar labels indicate the percentage reductions.

5.3 Fuselage surface pressure during wake encounter

In addition to the rotor load variation, the pressure distribution on the fuselage surface is examined to evaluate the airframe loading induced by wake encounter. Fig. 14 compares the pressure-coefficient distributions on the fuselage surfaces of the leading and following aircraft at different advance ratios and vertical separation distances.

The left and right columns correspond to μ = 0.15 and 0.23, respectively. Fig. 14(a) corresponds to the leading aircraft, whereas Figs. 14(b)–(d) pertain to the following aircraft at z/R = 0, −1, and −2, respectively. For the leading aircraft, both advance ratios result in similar pressure patterns, with a positive pressure region near the nose and rotor cowling regions and a negative pressure region over the upper and rear fuselage. This distribution represents the typical airframe pressure loading in forward flight, including nose stagnation, flow acceleration over the upper fuselage, and rotor-induced flow near the rotor support structures.

The pressure field of the following aircraft is substantially modified when the convected wake from the leading aircraft reaches the fuselage and rotor support structures. At z/R = 0 (Fig. 14(b)), the pressure coefficient distribution becomes more irregular than that of the leading aircraft for both advance ratios. This change is particularly evident over the upper fuselage and tail boom, where the incoming wake distorts the local flow around the airframe. At μ = 0.15, the wake descends toward the following aircraft, producing a broader pressure distortion over the upper fuselage. At μ = 0.23, the stronger streamwise convection shifts the wake encounter region, resulting in a different distribution of positive and negative pressure regions along the fuselage. These patterns are consistent with the wake encounter characteristics shown in Fig. 10, indicating that the following fuselage experiences a strongly nonuniform flow field during wake encounter.

The effect of vertical separation is more evident in Figs. 14(c) and 14(d). At z/R = −1, the following aircraft at μ = 0.15 still exhibits noticeable pressure distortion because the leading-aircraft wake remains close to the upper fuselage and rotor support region. In contrast, at μ = 0.23, the pressure variation becomes weaker because the main wake region convects farther downstream and remains above the following aircraft. At z/R = −2, the pressure distribution gradually recovers toward the baseline pattern of the leading aircraft. In particular, Case 6 (Fig. 14(d), right) shows the closest agreement with the leading-aircraft pressure distribution because the following aircraft is positioned largely outside the main wake encounter region.

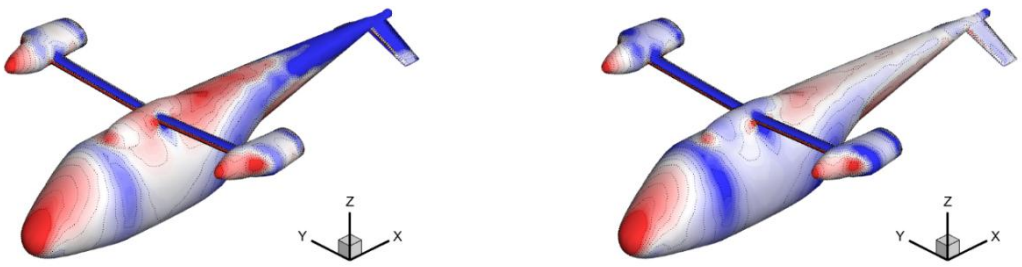

(a)

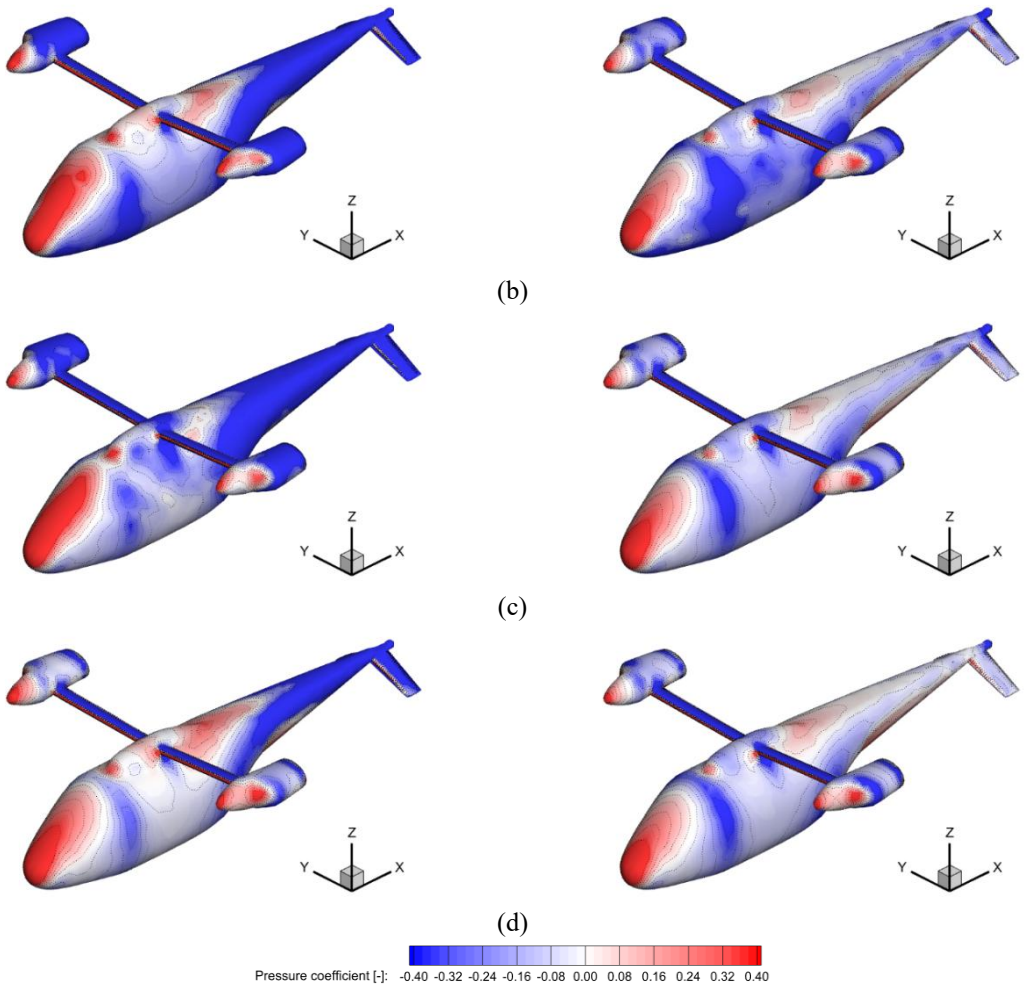

Fig. 14. Instantaneous pressure coefficient distributions on the fuselage surfaces of the leading and following aircraft during wake encounter. The left and right columns correspond to $\mu = 0.15$ and 0.23, respectively: (a) leading rotor, (b) following rotor at $z/R = 0$, (c) following rotor at $z/R = -1$, and (d) following rotor at $z/R = -2$.

The instantaneous pressure contours in Fig. 14 show localized irregular pressure distributions over the fuselage surface under wake encounter conditions. To quantify the temporal variation, the pressure-coefficient distributions are extracted along the longitudinal section at $y/R = 0$. Fig. 15(a) shows the longitudinal section, and Fig. 15(b) defines the upper and lower surface portions used for the pressure extraction. The pressure coefficient is plotted as a function of x/L, where L denotes the fuselage length. Fig. 16 presents the mean pressure coefficient distributions together with the maximum and minimum ranges over the last rotor revolution. The left and right columns correspond to $\mu = 0.15$ and 0.23, respectively. For the upper surface (Fig. 16(a)), the leading fuselage provides the baseline pressure distribution, with a higher pressure coefficient near the forward fuselage and lower pressure levels over the mid and rear fuselage regions. The mean pressure distributions of the following fuselage remain comparable to that for the leading fuselage, although clear deviations appear in several cases, particularly

at μ = 0.15. At μ = 0.15, Case 2 (z/R = −1) shows the most pronounced deviation from the leading-fuselage distribution over the mid and rear fuselage regions, and the maximum–minimum range is considerably wider than those in Cases 1 and 3. This indicates that wake encounter produces a more unsteady pressure response on the upper fuselage when the convected wake passes near the centerline section. This behavior is consistent with the irregular surface-pressure pattern observed in Fig. 14. Moreover, the enlarged maximum–minimum range in Fig. 16 indicates that the pressure disturbance is associated with temporal pressure variation over the last rotor revolution. At μ = 0.23, the deviation in the mean pressure level is smaller than that at μ = 0.15. However, Case 4 shows a more substantial temporal pressure variation than those in Cases 5 and 6, especially over the forward and aft portions of the upper surface. This indicates that even at the higher advance ratio, the same-altitude condition produces an unsteady pressure response on the upper surface, although the overall deviation from the leading fuselage distribution is smaller than that observed in Case 2. Cases 5 and 6 remain closer to the baseline distribution and show smaller fluctuation ranges over most of the upper surface.

For the lower surface (Fig. 16(b)), pressure fluctuation trends appear more consistent. Differences in the mean pressure coefficient between the leading and following fuselages remain limited over most of the lower surface. By contrast, the fluctuation range increases when the convected wake passes close to the centerline section. At μ = 0.15, Case 2 again shows the largest temporal variation, especially over the aft lower surface, while the fluctuation level decreases in Case 3 as the following aircraft moves farther from the main wake region. At μ = 0.23, Case 4 exhibits the largest temporal variation on the lower surface, particularly over the forward and mid fuselage regions. In contrast, Cases 5 and 6 show narrower fluctuation ranges and remain closer to the leading-fuselage distribution over most of the lower surface. These results indicate that the centerline pressure response is characterized primarily by an increase in temporal pressure fluctuation rather than by a large shift in the mean pressure distribution. The enlarged maximum–minimum ranges in Cases 2 and 4 indicate that the pressure unsteadiness becomes more pronounced when the convected wake passes close to the fuselage centerline. To quantify the fuselage surface-pressure variations shown in Fig. 16, the absolute difference in the mean pressure coefficient between the leading and following aircraft was calculated at each x/L location and length-averaged using trapezoidal integration. As summarized in Table 14, Case 2 at μ = 0.15 showed the largest differences, with values of 0.506 and 0.191 on the upper and lower surfaces, respectively. At the largest vertical separation, these differences decreased to 0.117 and 0.047 in Case 3. At μ = 0.23, the corresponding differences decreased from 0.082 and 0.103 in Case 4 to 0.025 and 0.012 in Case 6. Such an unsteady pressure response can contribute to unsteady airframe loading and aerodynamic moment response, as discussed in the following section.

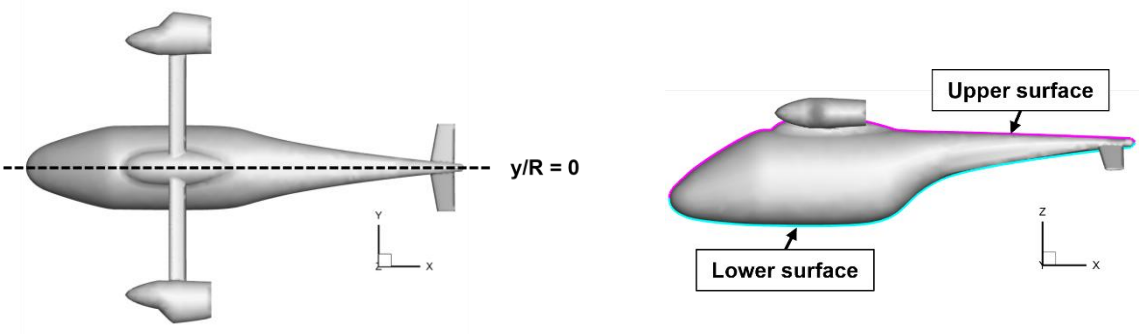

(a) (b)

Fig. 15. Longitudinal section used for the fuselage pressure coefficient analysis: (a) top view showing the section at $y/R = 0$ and (b) side view defining the upper and lower surface portions of the section.

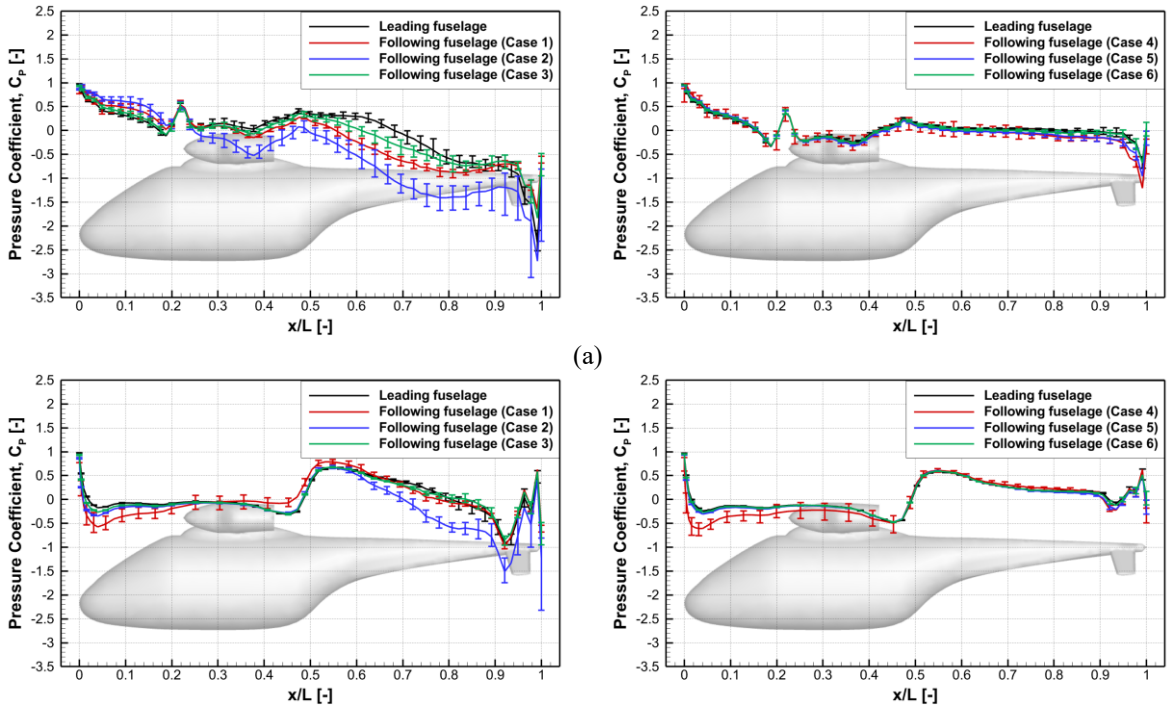

(a)

(b)

Fig. 16. Mean pressure coefficient distributions with maximum and minimum ranges over the last rotor revolution on the fuselage longitudinal section at $y/R = 0$. The left and right columns correspond to $\mu = 0.15$ and 0.23, respectively: (a) upper surface and (b) lower surface.

Table 14. Mean absolute differences in fuselage pressure coefficient between the leading and following aircraft.

Case	Upper surface [-]	Lower surface [-]
1	0.234	0.131
2	0.506	0.191
3	0.117	0.047
4	0.082	0.103
5	0.072	0.029
6	0.025	0.012

5.4 Pitching moment response of the following aircraft

The pitching moment response is examined to evaluate the longitudinal aerodynamic disturbance imposed on the following aircraft during wake encounter. While the preceding analyses separately quantify rotor thrust degradation and fuselage pressure variation, the pitching moment provides an integrated measure of their influence on longitudinal load balance. This quantity is especially important because wake-induced changes in rotor loading and airframe pressure can induce an unsteady pitching moment, thereby altering the longitudinal aerodynamic loading of the following aircraft. In this analysis, the pitching moment is decomposed into rotor and fuselage contributions to identify the aerodynamic sources of the moment variation. The rotor contribution represents the effect of thrust variation and azimuthal load redistribution over the rotor disks, whereas the fuselage contribution represents the effect of wake-induced pressure fluctuation over the airframe surfaces. Fig. 17 shows the time histories of the rotor and fuselage pitching moments for different advance ratios and vertical separation distances. The left and right columns correspond to μ = 0.15 and 0.23, respectively, and Figs. 17(a) and 17(b) show the rotor and fuselage contributions, respectively. The pitching moment is evaluated about the midpoint between the centers of the two rotors. The sign convention follows the coordinate system defined in Section 4, with positive and negative pitching moments denoting nose-up and nose-down rotations, respectively.

Fig. 17(a) shows the rotor pitching moment. For the leading aircraft, the mean value remains nearly constant at both advance ratios, with only small periodic variations. By contrast, the following aircraft exhibits a pronounced shift toward negative pitching moment after the leading-aircraft wake reaches the rotor disk region. At μ = 0.15, Case 1 shows the largest negative shift because the following rotors are directly exposed to the main wake at the same altitude. The initial positive shift before the rapid decrease in moment corresponds to the transient thrust increase observed in Fig. 11(a), whereas the subsequent negative shift results from the thrust loss and azimuthal load redistribution observed in Fig. 12. As the following aircraft is displaced downward in Cases 2 and 3, wake ingestion by the rotors is reduced, and the rotor pitching moment approaches that of the leading rotor. At μ = 0.23, the same trend is observed; however, the vertical separation exerts a more notable effect. Case 4 shows a distinct negative moment shift, whereas Cases 5 and 6 exhibit levels approaching the leading rotor moment; this is because the main wake region passes farther above the following rotor disks.

The fuselage pitching moment (Fig. 17(b)) exhibits a different dependence on vertical separation. The most notable variation appears in Case 2 at μ = 0.15, where the fuselage pitching moment becomes more negative and exhibits the largest unsteady fluctuation among Cases 1–3. This behavior is consistent with the pressure coefficient

analysis in Figs. 14 and 16: the downward-displaced wake at μ = 0.15 interacts strongly with the upper fuselage and rotor support structures when the following aircraft is located one rotor radius below the leader. The increased pressure fluctuation along the fuselage centerline produces unsteady airframe loading, resulting in large variations in the fuselage pitching moment. At μ = 0.23, Cases 4 and 5 show larger fuselage moment changes than those in Case 6. In Case 4, the following fuselage is directly exposed to the convected wake at the same altitude, while in Case 5, the wake produces the strongest centerline pressure fluctuation. In Case 6, the wake influence on the fuselage is substantially reduced, and the fuselage pitching moment approaches that of the leading aircraft.

The mean rotor and fuselage pitching moments over the last rotor revolution are summarized in Table 15. At μ = 0.15, the rotor pitching moment of the following aircraft decreased by 4000, 1163, and 681 Nm relative to that of the leading aircraft in Cases 1–3, respectively. At μ = 0.23, the corresponding decreases were 2609, 148, and 80 Nm in Cases 4–6. In contrast, the fuselage pitching moment showed a different trend. At μ = 0.15, the largest difference from the leading aircraft was 2302 Nm in Case 2, whereas at μ = 0.23, the difference decreased from 1619 Nm in Case 4 to 413 Nm in Case 6. These quantitative comparisons further clarify the different trends of the rotor and fuselage pitching moments observed in Fig. 17.

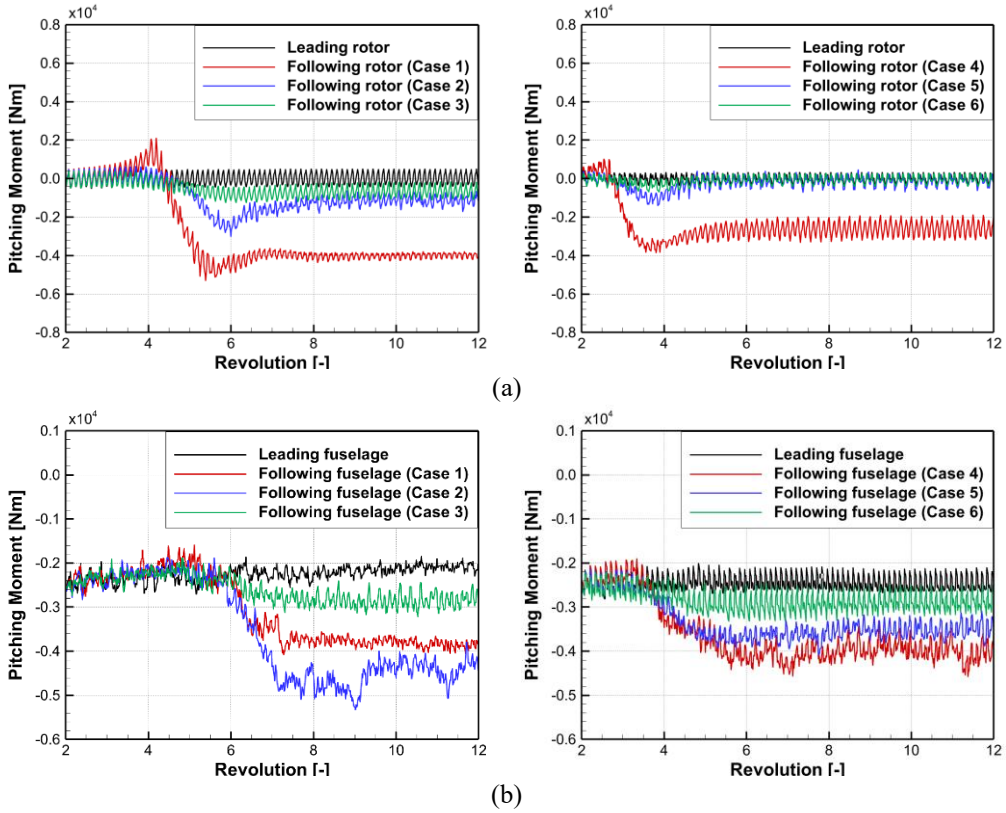

Fig. 17. Time histories of rotor and fuselage pitching moments for the leading and following aircraft during wake encounter. The left and right columns correspond to μ = 0.15 and 0.23, respectively: (a) rotor pitching moment and (b) fuselage pitching moment.

Table 15. Mean rotor and fuselage pitching moments of the leading and following UAM aircraft.

Case	Leading rotor [Nm]	Following rotor [Nm]	Leading fuselage [Nm]	Following fuselage [Nm]
1		-3980		-3859
2	20	-1143	-2144	-4446
3		-661		-2831
4		-2587		-4078
5	22	-126	-2459	-3482
6		-58		-2872

6. Conclusions

Wake encounter characteristics between two full-configuration side-by-side UAM aircraft in forward flight were examined using an in-house aerodynamic framework based on vortex method. The numerical method was validated using the induced velocity field for a single rotor wake and the tip vortex trajectories of the ROBIN helicopter model, confirming that the solver can reasonably predict rotor wake structures and tip vortex motion during forward flight. The validated solver was applied to six wake encounter cases defined by two advance ratios, $\mu = 0.15$ and 0.23, and three vertical separation distances, $z/R = 0$, -1, and -2, at a fixed streamwise separation of $x/R = 6$.

The wake behavior and its interaction with the following aircraft were affected by both the advance ratio and vertical separation distance. At the lower advance ratio, the wake of the leading aircraft was displaced farther downward, and its influence persisted even when the following aircraft was located below the leading aircraft. At the higher advance ratio, the wake convected farther downstream, and the interaction between the wake and the following aircraft weakened with increasing vertical separation. The rotor loads of the following aircraft were reduced with intensifying interaction of the leading-aircraft wake with the rotor disks. The thrust reduction was the largest under the same-altitude condition and decreased with increasing vertical separation at both advance ratios. By contrast, the torque reduction was considerably smaller than the thrust reduction and showed a different dependence on the advance ratio and vertical separation. At the higher advance ratio, the torque reduction decreased with increasing vertical separation, whereas this trend was not observed at the lower advance ratio.

The fuselage pressure response depended on the position of the wake relative to the following aircraft, which varied with the advance ratio and vertical separation. At the lower advance ratio, the wake was displaced farther downward, leading to more pronounced changes in the pressure coefficient distributions over the upper and rear fuselage regions. At the higher advance ratio, the pressure distributions of the following aircraft remained closer

to those of the leading aircraft because the wake convected farther downstream. The pitching moment response differed between the rotor and fuselage contributions. The rotor pitching moment was mainly related to the thrust reduction and thrust distribution over the rotor disks, whereas the fuselage pitching moment was more sensitive to unsteady variations in the fuselage surface pressure.

The aerodynamic response during wake encounters was not governed only by the geometric separation between the aircraft; it also varied with the wake trajectory and the position of the wake relative to the following aircraft, both of which were affected by the advance ratio. These findings can provide an aerodynamic basis for future assessments of UAM separation and operational safety. However, extending the present results to specific operational separation criteria requires further evaluation over broader ranges of advance ratio and streamwise and vertical separation. Future work will extend the VPM to include viscous diffusion and further consider turbulence effects to represent wake evolution under more realistic UAM operating conditions.

Declaration of competing interest

The authors declare that they have no competing financial interests or personal relationships that may have influenced the work reported in this study.

Acknowledgments

This work was supported by the National Research Foundation of Korea (NRF) grant funded by the Ministry of Science and ICT (Project No. RS-2025-25423496) and the Glocal University 30 Project Fund of Gyeongsang National University in 2026.

References

[1] W.J. Mccroskey, Vortex wakes of rotorcraft, 33rd Aerospace Sciences Meeting and Exhibit (1995) 530. https://doi.org/10.2514/6.1995-530

[2] J. Cho, B.J. Lee, T. Misaka, K. Yee, Study on decay characteristics of vertical four-vortex system for increasing airport capacity, Aerosp. Sci. Technol. 105 (2020) 106017. https://doi.org/10.1016/j.ast.2020.106017.

[3] H. Gao, C. Liu, Y. Chen, X. He, Research on wake interval of paired departure at closely spaced parallel runways, Qual. Reliab. Eng. Int. 39 (2023) 1935–1951. https://doi.org/10.1002/qre.3338.

[4] International Civil Aviation Organization, Procedures for air navigation services (PANS) - air traffic management, ICAO Doc. 4444 Amendment 9, 2020.

[5] Federal Aviation Administration, Order JO 7110.65BB air traffic control, U.S. Department of Transportation, Federal Aviation Administration, 2025.

[6] F. Rooseleer, "RECAT-EU" European wake turbulence categorisation and separation minima on approach and departure edition number: 2.0, 2024. https://www.eurocontrol.int/publication/european-wake-turbulence-categorisation-and-separation-minima-approach-and-departure

[7] European Union Aviation Safety Agency, Easy access rules for air traffic management/air navigation services — provision of services (Regulation (EU) 2017/373), 2025. https://www.easa.europa.eu/en/document-library/easy-access-rules/easy-access-rules-air-traffic-managementair-navigation-services-provision-services

[8] EUROCONTROL, RECAT-EU-PWS wake turbulence separation scheme: optimised wake turbulence categorisation and static pair-wise separation minima on approach and departure, Edition 2.0, 2023. https://www.eurocontrol.int/publication/recat-eu-pws-scheme

[9] J.E. Baculi, N.T. Nguyen, W. Okolo, J. Xiong, Wake disturbance-based separation evaluation for urban air mobility aircraft, in: AIAA AVIATION FORUM AND ASCEND 2024, 2024: p. 3771.

[10] M. Radotich, Conceptual design of tiltrotor aircraft for urban air mobility, in: Aeromechanics for Advanced Vertical Flight Technical Meeting, Transformative Vertical Flight 2022, 2022.

[11] S. Dougherty, N.L. Oo, D. Zhao, Effects of propeller separation and onset flow condition on the performance of quadcopter propellers, Aerosp. Sci. Technol. 145 (2024) 108837. https://doi.org/10.1016/j.ast.2023.108837.

[12] A. Zanotti, A. Velo, C. Pepe, A. Savino, D. Grassi, L. Riccobene, Aerodynamic interaction between tandem propellers in eVTOL transition flight configurations, Aerosp. Sci. Technol. 147 (2024) 109017. https://doi.org/10.1016/j.ast.2024.109017.

[13] C. Liu, B. Li, Z. Wei, Z. Zhang, Z. Shan, Y. Wang, Effects of wake separation on aerodynamic interference between rotors in urban low-altitude UAV formation flight, Aerospace 11 (2024) 865.

https://doi.org/10.3390/aerospace11110865.

[14] S. Yoon, H.C. Lee, T.H. Pulliam, Computational analysis of multi-rotor flows, in: 54th AIAA Aerospace Sciences Meeting, 2016: p. 0812. https://doi.org/10.2514/6.2016-0812

[15] J.Y. Hwang, M.K. Jung, O.J. Kwon, Numerical study of aerodynamic performance of a multirotor unmanned-aerial-vehicle configuration, J. Aircr. 52 (2015) 839–846. https://doi.org/10.2514/1.C032828.

[16] P. Ventura Diaz, W. Johnson, J. Ahmad, S. Yoon, Computational study of the side-by-side urban air taxi concept, in: Vertical Flight Society's (VFS) Annual Forum and Technology Display, 2019.

[17] E.J. Alvarez, A. Ning, High-fidelity modeling of multirotor aerodynamic interactions for aircraft design, AIAA J. 58 (2020) 4385–4400. https://doi.org/10.2514/1.J059178.

[18] D.G. Caprace, A. Ning, P. Chatelain, G. Winckelmans, Effects of rotor-airframe interaction on the aeromechanics and wake of a quadcopter in forward flight, Aerosp. Sci. Technol. 130 (2022) 107899. https://doi.org/10.1016/j.ast.2022.107899.

[19] D.-G. Caprace, A. Ning, Large eddy simulation for empirical modeling of the wake of three urban air mobility vehicles, J. Am. Helicopter Soc. 68 (2023) 42002–42017. https://doi.org/10.4050/JAHS.68.042002

[20] M.S. Araghizadeh, B. Sengupta, H. Lee, R.S. Myong, Aeroacoustic investigation of side-by-side urban air mobility aircraft in full configuration with ground effect, Phys. Fluids 36 (2024) 087160. https://doi.org/10.1063/5.0221902.

[21] A. Stephan, S. Zholtovski, F. Holzäpfel, Formation flight and wake vortex encounters with fully coupled hybrid rans/les, in: AERO2020+ 1 55th 3AF International Conference on Applied Aerodynamics, 3AF, 2021.

[22] G. Höhne, M. Fuhrmann, R. Luckner, Critical wake vortex encounter scenarios, Aerosp. Sci. Technol. 8 (2004) 689–701. https://doi.org/10.1016/j.ast.2004.07.005.

[23] G. Querinjean, V. Colognesi, M. Duponcheel, G. Poncelet, D.-G. Caprace, P. Chatelain, G. Winckelmans, Large eddy simulation of an advancing rotor for the characterization of wake signature and wake encounter severity on final approach, in: 50th European Rotorcraft Forum, 2024.

[24] B. Lawrence, G.D. Padfield, Wake vortex encounter severity for rotorcraft in final approach, Aerosp. Sci. Technol. 12 (2008) 385–397.

[25] C.H.J. Wang, K.H. Low, Software-in-the-loop investigation of wake-vortex-encounter-response of identical multirotor pair with PX4 attitude controller, Aerosp. Sci. Technol. 117 (2021) 106967. https://doi.org/10.1016/j.ast.2021.106967.

[26] H.H. Heyson, S. Katzoff, Induced velocities near a lifting rotor with nonuniform disk loading, NACA-TR-1319, 1957.

[27] T.A. Ghee, J.D. Berry, L.A.J. Zori, J.W. Elliott, Wake geometry measurements and analytical calculations on a small-scale rotor model, NASA Technical Paper 3584, ATCOM TR-96-A-007, NASA Langley Research Center, 1996.

[28] J. Katz, A. Plotkin, Low-Speed Aerodynamics: From Wing Theory to Panel Methods, McGraw-Hill, New York, 1991.

[29] H. Lee, D.J. Lee, Numerical investigation of the aerodynamics and wake structures of horizontal axis wind turbines by using nonlinear vortex lattice method, Renew. Energy 132 (2019) 1121–1133. https://doi.org/10.1016/j.renene.2018.08.087.

[30] H. Lee, D.J. Lee, Rotor interactional effects on aerodynamic and noise characteristics of a small multirotor unmanned aerial vehicle, Phys. Fluids 32 (2020) 047107. https://doi.org/10.1063/5.0003992.

[31] M.S. Araghizadeh, B. Sengupta, S.M. Son, H. Lee, R.S. Myong, Atmospheric turbulence inflow effect on the aerodynamics and aeroacoustics of side-by-side urban air mobility aircraft, Phys. Fluids 37 (2025) 107105. https://doi.org/10.1063/5.0288862.

[32] S.M. Son, C.H. Song, M.S. Araghizadeh, R.S. Myong, H. Lee, Investigation of aerodynamics, wake dynamics, and aeroacoustic characteristics of a full-configuration tiltrotor aircraft during transition flight, Phys. Fluids 37 (2025) 107133. https://doi.org/10.1063/5.0296874.

[33] H. Lee, D.J. Lee, Wake impact on aerodynamic characteristics of horizontal axis wind turbine under yawed flow conditions, Renew. Energy 136 (2019) 383–392. https://doi.org/10.1016/j.renene.2018.12.126.

[34] H. Lee, B. Sengupta, M.S. Araghizadeh, R.S. Myong, Review of vortex methods for rotor aerodynamics and wake dynamics, Adv. Aerodyn. 4 (2022). https://doi.org/10.1186/s42774-022-00111-3.

[35] C. He, J. Zhao, Modeling rotor wake dynamics with viscous vortex particle method, AIAA J. 47 (2009) 902–915. https://doi.org/10.2514/1.36466.

[36] A. Gessow, A.D. Crim, A method for studying the transient blade-flapping behavior of lifting rotors at extreme operating conditions, NACA-TN-3366, 1955.

[37] T.A. Egolf, A.J. Landgrebe, Helicopter rotor wake geometry and its influence in forward flight. Volume 1: generalized wake geometry and wake effect on rotor airloads and performance, NASA-CR-3726, UTRC/R83-912666-58-VOL-1, 1983.

[38] A.R. Kenyon, R.E. Brown, Wake dynamics and rotor-fuselage aerodynamic interactions, J. Am. Helicopter Soc. 54 (2009) 12003. https://doi.org/10.4050/JAHS.54.012003.

[39] C. Silva, W. Johnson, K.R. Antcliff, M.D. Patterson, VTOL urban air mobility concept vehicles for technology development, in: 2018 Aviation Technology, Integration, and Operations Conference, AIAA AVIATION Forum, 2018, AIAA 2018-3847. https://doi.org/10.2514/6.2018-3847

[40] W. Johnson, C. Silva, NASA concept vehicles and the engineering of advanced air mobility aircraft, Aeronaut. J. 126 (2022) 59–91. https://doi.org/10.1017/aer.2021.92.

[41] S.J. Wright, H. V Cummings, Pretest comprehensive analysis for the urban air mobility side-by-side test stand, in: Aeromechanics for Advanced Vertical Flight Technical Meeting, Transformative Vertical Flight 2022, 2022.

[42] U.S. Department of the Air Force, Air Force Manual 11-2TH-1H, Volume 3: TH-1H Helicopter Operations Procedures, 2020. https://static.e-publishing.af.mil/production/1/af_a3/publication/afman11-2th-1hv3/afman11-2th-1hv3.pdf